IMAGING OF FLOW PATTERNS WITH MOLECULAR ROTORS

by

ADNAN MUSTAFIC

(Under the direction of Mark A. Haidekker)

ABSTRACT

Molecular rotors are fluorescent molecules used as non-mechanical microviscosity sensors with high spatial and temporal resolution. They form twisted intramolecular charge transfer (TICT) states, and once photoexcited they return to their ground states following one of two de-excitation pathways: nonradiative intramolecular rotation or fluorescence emission. A recent discovery has shown an increase in the shearing rate of a viscous solvent containing molecular rotors leads to an increasing quantum yield, and new research was conducted to better understand this phenomena. Viscous solvents containing molecular rotors were injected into different chamber geometries, with flow rates were controlled by a syringe pump. Collimated LEDs provided the light source necessary to photoexcite fluorescent molecules. A biomedical imaging software was used to analyze images, and the analysis shows a good visual match with CFD patterns, and thereby manifests promising signs for the use of molecular rotors as highly sensitive shear stress imaging and flow pattern sensors.

INDEX WORDS: Molecular Rotors, Shear Stress, Flow Sensors, Twisted Intramolecular Charge Transfer States, Microfluidics

IMAGING OF FLOW PATTERNS WITH MOLECULAR ROTORS

by

ADNAN MUSTAFIC

B.S., The University of Missouri, 2007

A Thesis Submitted to the Graduate Faculty
of The University of Georgia in Partial Fulfillment
of the
Requirements for the Degree

MASTER OF SCIENCE

ATHENS, GEORGIA

2009

Imaging of Flow Patterns With Molecular Rotors

by

Adnan Mustafic

Approved:

Major Professor:	Mark A. Haidekker
Committee:	William S. Kisaalita Peter A. Kner

Electronic Version Approved:

Maureen Grasso
Dean of the Graduate School
The University of Georgia
December 2009

ACKNOWLEDGMENTS

I would like to acknowledge Dr. Mark Haidekker for guidance and support throughout this project. I'd like to extend acknowledgments to committee members William Kisaalita and Peter Kner, Darcy Lichlyter for help in lab, and Hsuan-Ming Huang for help with CFD images.

TABLE OF CONTENTS

Page

CHAPTER

Appendix

List of Figures

List of Tables

LIST OF ABBREVIATIONS AND SYMBOLS

TICT- Twisted Intramolecular Charge Transfer

L_a, L_b-orbital configurations of local states

MRI-Magnetic Resonance Imaging

DMABN-dimethylamino-benzonitrile

DMASP-4-[4-(dimethylamino)styryl]pyridine

CCVJ-[9-(2-carboxy-2-cyanovinyl)-julolidine]

CCVJ-TEG-[9-(2-carboxy-2-cyanovinyl)-julolidine triethyleneglycol ester]

DCVJ-[9-(2,2-dicyano-vinyl)-julolidine]

Diol-(p-[(2-cyano-2-propanediol ester)vinyl]dimethylaniline)

EG-Ethylene Glycol

TPM-triphenylmethane

LED-Light Emitting Diode

CFD-Computer Fluid Dynamics

LIF-Laser Induced Fluorescence

TICT-Twisted intramolecular charge transfer

ICT-Intramolecular charge transfer

LE-Locally excited

WLF Model-Williams Landel Ferry Model

μ-Dynamic viscosity

τ-Shear Stress

$\frac{dx}{dy}$-Fluid Velocity Gradient

ϕ-Fluorescent Quantum Yield

η-Solvent Viscosity

η_c-Characteristic Solvent Viscosity

λ-Wavelength

ξ-Proportionality Constant of Corrected Factors

ϵ- Dielectric constant

x-Dye Dependant Constant

C-Förster-Hoffmann Proportionality Constant

v-Fluid Velocity

v_c-Characteristic Fluid Velocity

k_f, k_{nf}-radiative fluorescence decay rate and non-radiative fluorescence decay rates for LE excited state

k'_f, k'_{nf}-radiative fluorescence decay rate and non-radiative fluorescence decay rates for TICT state

k_a-constant for forward reaction of TICT formation

k_d-constant for backward reaction from TICT to LE state

$V_j\,(\phi_1 + \phi_2 + \phi_3)$-electrostatic potential equation for states S0, S1, S3

I_{em}, I_{ab}-emission intensity, absorbed light intensity

CHAPTER 1

FLUORESCENCE

Emission of light from a substance occurs from excited states, and this phenomena is called luminescence. There exist two subgroups of luminescence: fluorescence and phosphorescence, and this division depends on the characteristics of their excited states. Fluorescence occurs when an electron in the excited singlet state (S1, S2) from an excited orbital is paired with an electron from the ground state orbital (S0). The return to the ground state is accompanied with a photon emission rate of $\approx 10^8 s^{-1}$. Molecules in the S1 state can undergo a spin conversion to triplet state T1, and emission from T1 state is called phosphorescence.

The processes occuring between the light absorption and emission are described by Jablonski's diagram in Figure 1.1. Vertical lines represent transitions between states. These transitions which last $\approx 10^{-15}$ seconds without a nuclei displacement are described by the Franck-Condon principle [1].

The average time a molecule spends in the excited state before returning to the ground state is called lifetime, and can be expressed with:

$$\tau = \frac{1}{\Gamma + k_{nr}} \tag{1.1}$$

where Γ is the flurophore emission rate, and k_{nr} is the non-radiative decay to ground state S0. Typical fluorescence lifetime is about 10 ns, whereas phosphorescence lifetime is on the order of milliseconds to seconds. The flurophore lifetime in the absence of non-radiative processes is called natural lifetime and can be expressed with:

$$\tau_n = \frac{1}{\Gamma} \tag{1.2}$$

or in the terms of lifetime from Equation 1.1:

$$\tau_n = \frac{\tau}{Q} \tag{1.3}$$

where Q is the quantum yield. Quantum yield is the number of emitted photons relative to the number of absorbed photons:

$$Q = \frac{\Gamma}{\Gamma + k_{nr}}. \tag{1.4}$$

For cases when $k_{nr} << \Gamma$, quantum yield approaches unity [1].

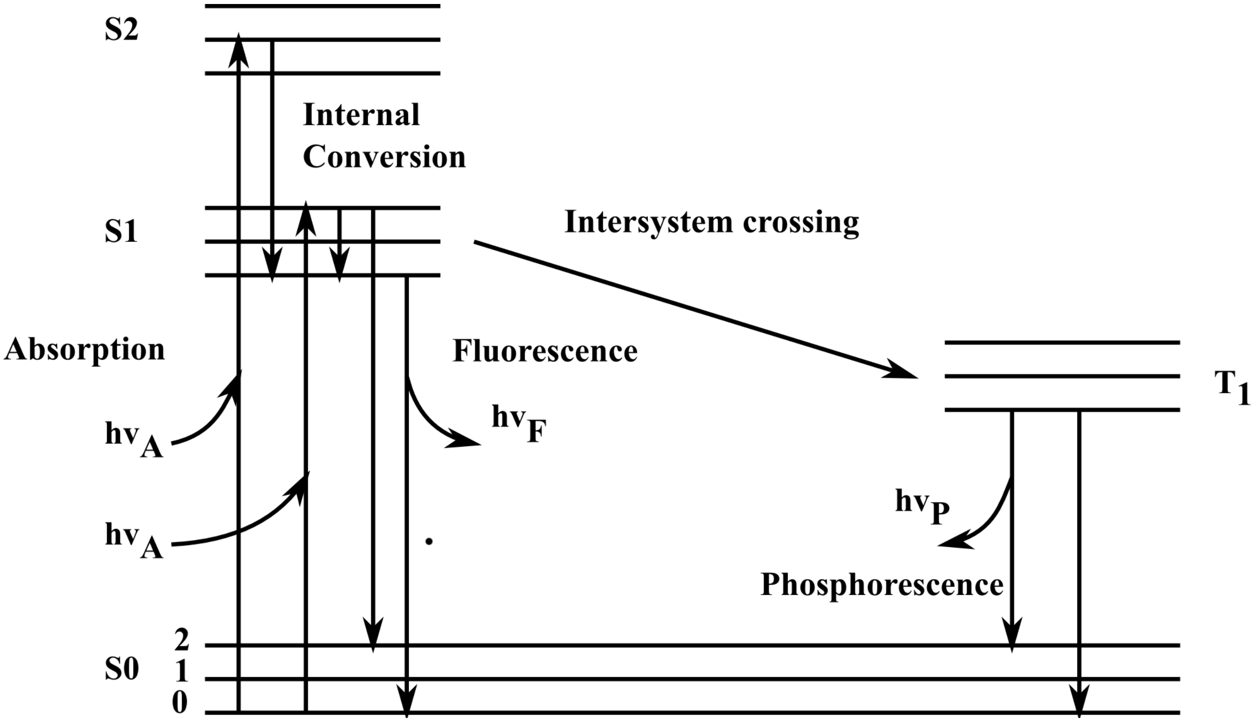

Figure 1.1: Jablonski diagram and relative positions of absorption, fluorescence, and phosphorescence spectra. Vertical lines describe transitions between state. S0-singlet ground state, S1, S2- first and second excited states. Adapted from [1].

Chapter 2

Introduction to Molecular Rotors

In 1962, Lippert et al. reported the presence of a dual fluorescence emission in p-N,N-dimethylamino-benzonitrile (DMABN)(chemical structure shown in Figure 2.1) when mixed with polar solvents, but not in non-polar solvents [2]. Beside a regular fluorescence emission, another bathochromic (red-shifted) fluorescence emission with a longer wavelength was recorded, and the question emerged on what was the underlying photophysical principle behind the second emission. Lippert et al. hypothesized that this occurence was due to solvent polarity affecting the locally emitting L_a (more polar) and L_b (less polar) states, or a diatomic excimer formed from two molecules, one from the solvent and the other one from DMABN in the excited state [14].

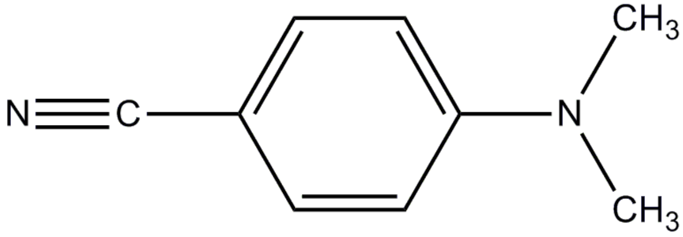

Figure 2.1: Chemical Structure of p-N,N-dimethylamino-benzonitrile

In 1973, Grabowski et al. suggested that Twisted Intramolecular Charge Transfer (TICT) states form following the photoexcitation of the fluorescent molecule in a polar solvent, and locally emitting states or the diatomic excimer were not responsible for this phenomena. He found that the fluorescence anisotropies of dual fluorescence bands was positive and not negative (originally predicted by Lippert), and the twisting of the diamino group occured in other DMABN derivatives [3]. Grabowski et al. hypothesized that when DMABN is photoexcited, dimethylamino group twists with respect to the ring, with former becoming an electron donor group and latter an electron acceptor group [15].

In Figure 2.2 the configurations of DMABN at different states are shown. In ground state, the dimethylamino and the benzonitrile group are in plane, and following ultraviolet excitation (λ_{exc}=266 nm) to locally excited state LE (or L_b), the dimethylamino group twists by 30°. In non-polar solvents DMABN returns to ground state (λ_{em}=345 nm) or in polar solvents (acetonitrile) forms a TICT state in about 6 picoseconds. Once it forms the TICT state, the dimethylamino group is twisted 90° around its rotational axis with respect to the benzonitrile group. At this point, nitrogen donates an electron to the ring, thus increasing the methyl group(s) rotation, and after the end of photoexcitation returns to ground state (λ_{em}=500 nm).

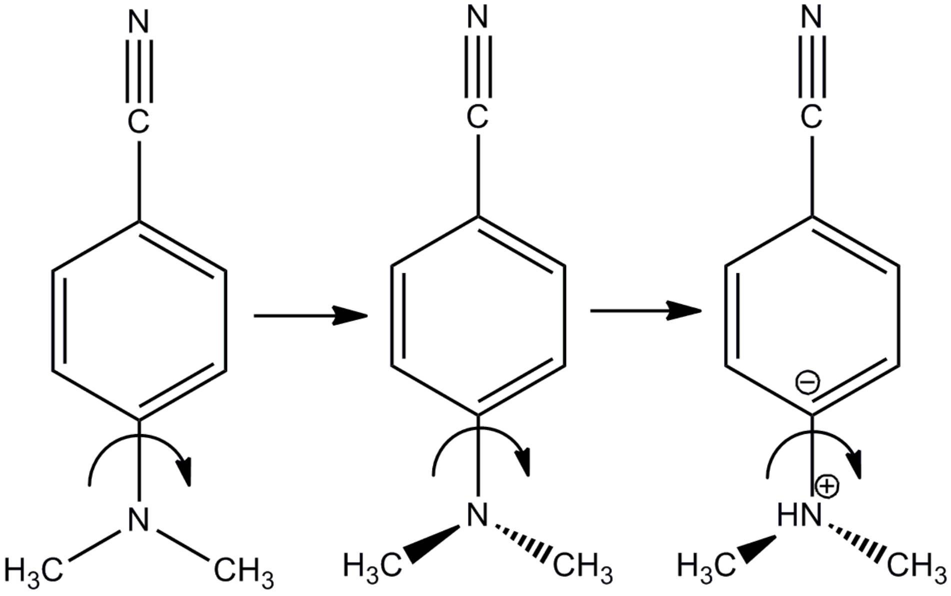

1 **2** **3**

Figure 2.2: Excited states of p-N,N-dimethylamino-benzonitrile in acetonitrile. Arrows denote the rotationary axis when a fluorescent molecule in a viscous solvent is photoexcited, α is the angle of rotation between the dimethylamino and the benzonitrile group. In ground state (1) α=0°, excited state LE (or L_b) (2) α=30°, twisted intamolecular charge transfer state (3) α=90°. Adapted from [2, 3].

Examination of the picosecond time-resolved resonance Raman spectrum of the DMABN TICT state in a polar solvent has shown presence of an isosbestic point. Isosbestic point is found in an absorption spectrum when a fluorescent molecule (DMABN) and a solvent (acetonitrile) have constant and identical molar coefficients throughout the duration of a reaction, and its presence points to a reaction which occurs without formation of an intermediate product, thus negating the hypothesis of an excimer formation by Lippert et al [16, 17, 18].

In additional studies of the dual fluorescence emissions observed by Lippert et al., and quantified in terms of the TICT states discovered by Grabowski et al., the ratio of intensity of the TICT non-raditive decay and fluorescence intensity of the excited state can be related by:

$$\frac{I_{TICT}}{I_{LE}} = \frac{k'_f}{k_f} \cdot \frac{k_a}{k'_f + k'_{nf} + k_d} \tag{2.1}$$

where I_{TICT} is intensity of the TICT non-radiative decay, I_{LE} is fluorescence intensity of the excited state, k_f and k_{nf} are radiative fluorescence decay rate and non-radiative fluorescence decay rates for LE excited state, k'_f and k'_{nf} are radiative fluorescence decay rate and non-radiative fluorescence decay rates for TICT state, k_a is constant for forward reaction of TICT formation, k_d is rate constant for backward reaction from TICT to LE state (Figure 2.3) [5].

In solvents $k_d << k_a$ because of the lower level of S1 in the TICT state, the backward reaction rate k_d from TICT to LE state is negligible in comparison to the radiative and non-radiative decay rates for TICT state. Furthermore $k_d << k_f + k_{nf}$, and Equation 2.1 can be simplified to:

$$\frac{I_{TICT}}{I_{LE}} = \frac{k'_f}{k_f} \cdot \frac{k_a}{k'_f + k'_{nf}} \approx Ck_a \tag{2.2}$$

where $C = k'_f / k_f (k'_f + k'_{nf})$ and is a purely dye specific and solvent independent. The constant for forward reaction of TICT formation k_a can be expressed in terms of solvent viscosity:

$$k_a = A\eta^{-\alpha} exp(\frac{E_0}{k_B T}) \tag{2.3}$$

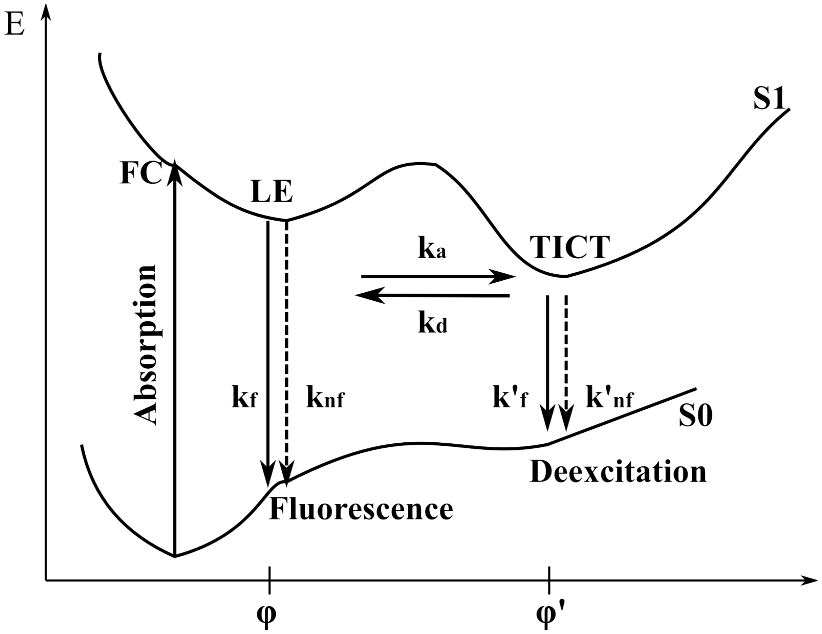

Figure 2.3: Schematic illustration of the potential energy surface of the singlet excited state S1 and the ground state S0 of a fluorescent molecule. Deexcitation from the locally excited state (LE) leads to a blue shifted emission peak, and higher energy change, while deexcitation from the TICT state leads to a red shifted emission peak and lower energy change. For DMABN φ=0, φ'=90 °. FC=Franck-Condon State, LE=equilibrious excited state. Adapted from [4, 5].

where A is viscosity independent constant, α is the relative importance of viscosity ($0.1< \alpha <1$), E_0 is the intrinsic activation energy, k_B is Boltzmann's constant, and T is temperature. The relative importance of the viscosity in the barrierless case when $\alpha \rightarrow 1$ and isomerization dynamics is mostly viscosity controlled, and $\alpha \rightarrow 0.1$ in cases when it's potential controlled [19]. For molecular rotors, the TICT formation process is a barrierless case because the activation barrier is smaller than the activation energy for solvent mobility, and therefore governed by the solvent viscosity [20, 21].

In the same study, the formation of TICT states with DMABN in polar viscous solvents was examined and findings point to a strong dependence between TICT formation and viscosity. The rate of formation was highest in glycerol and lowest in pentanol and butanol, while it didn't occur in non-polar solvents [22].

In this study, molecular rotors used were CCVJ (9-(2-carboxy-2-cyanovinyl)-julolidine) and Diol (p-[(2-cyano-2-propanediol ester)vinyl]dimethylaniline); their chemical structures are shown in Figure 2.4. After photoexcitation to a higher energy level, molecular rotors form TICT states, and return to their ground state following one of two de-excitation pathways: nonradiative molecular rotation or fluorescence emission. Unlike DMABN, CCVJ and Diol deexcite from the TICT state without photon emission [23].

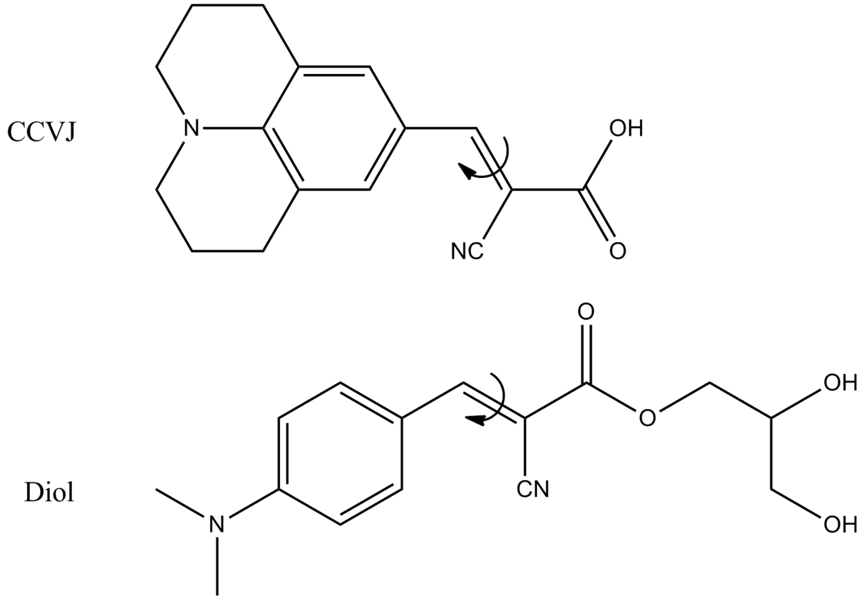

Figure 2.4: Chemical Structures of CCVJ (9-(2-carboxy-2-cyanovinyl)-julolidine) and Diol (p-[(2-cyano-2-propanediol ester)vinyl]dimethylaniline). Arrows around the C=C bond denote the axis of rotation when a molecular rotor in a viscous solvent is photoexcited.

Typically, molecular rotors consist of a nitrile group (electron acceptor group), and a julodine or dimethylamino headgroup (electron donor group for the intramolecular charge transfer) [24, 25]. The electron acceptor group may posses additional functional groups such as COOH, and can therefore be polar or non-polar, thus changing some of their chemical properties without changes of the photophysical properties [26, 21]. The optimal excitation range for molecular rotors is in the blue range (430-460 nm), while the optimal range for photon emission is in the green range (480-510 nm).

In solutions with low viscosity $k_f << k_a$, and the intramolecular rotation is the predominant de-excitation pathway, while in high viscosity solutions $k_f >> k_a$, the intramolecular rotation is impeded, and fluorescence emission is the predominant de-excitation pathway.In both CCVJ and Diol, the intramolecular rotation occurs arround the cyanovinyl bond[27, 28].

The wavelength difference between the maxima of the absorption and emission spectra is called the Stoke's shift, and for fluorescent molecular rotors represents an important descriptive property. Molecular rotors with longer Stoke's shift are preferred for fluorescence sensing and imaging because of an enhanced isolation of the excitation and emission light by optical filters. In those molecular rotors, the effects of re-absorption of emitted light, light scattering, and fluorescence quenching at high concentrations are smaller [29]. Stoke's shift for CCVJ and Diol is different solvents is shown in Table 2.1, where it's strongest for CCVJ in ethylene glycol and weakest in 1-nonanol, and strongest for Diol in DMSO and weakest in 1-nonanol.

Table 2.1: Stoke's shift for CCVJ and Diol dye in selected solvents

Molecular Rotor	Solvent	Measured Exc/Em (nm)	Stoke's Shift (nm)
CCVJ	Ethylene Glycol	422/486	64
	Methanol	425/485	60
	1-Nonanol	446/477	31
	DMSO	448/497	49
	Toluene	409/464	55
Diol	Ethylene Glycol	434/484	50
	Methanol	418/476	58
	1-Pentanol	432/468	36
	1-Nonanol	434/465	31
	DMSO	426/487	61
	Toluene	426/460	34

In 1971, Förster and Hoffmann examined another essential property of molecular rotors, their microviscosity sensitivity, and quantatively described the relation between viscosity and quantum yield [6]. They experimented with triphenylmethane (TPM) dyes, namely crystal violet and malachite green (chemical structures shown in Figure 2.5), and some of their derivatives which can be used as microviscosity sensors. Results showed that TPM dyes in low viscosity solvents exhibited lower quantum yield than that of TPM dyes in high viscosity solvents. The low quantum yield of TPM dyes was attributed to intramolecular rotation of the phenyl groups, and the relaxation time of intramolecular rotation depends on the solvent's viscosity.

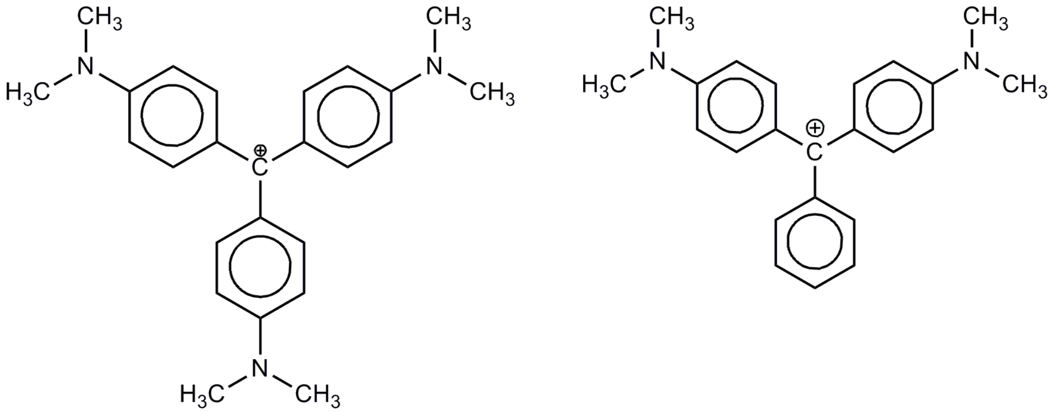

Crystal Violet

Malachite Green

Figure 2.5: Chemical Structures of Crystal Violet and Malachite Green. Phenyl groups undergo rotation around the central carbon during de-excitation from TICT to ground state.

Förster and Hoffmann described the electrostatic potential V$_j$ of TICT state forming TPM dyes in ground and excited states (S0, S1, S2) as:

$$V_j\left(\varphi_1+\varphi_2+\varphi_3\right)=\underbrace{\frac{1}{2}\alpha_j\left(\varphi_1^2+\varphi_2^2+\varphi_3^2\right)}_{A}-\underbrace{\sum_{i\neq k} f\left(\varphi_i+\varphi_k\right)}_{B} \tag{2.4}$$

where term A represents the electrostatic contribution of electrons from π bonds, and term B is the repulsion term of the phenyl groups. For constant α_j it is assumed that $\alpha_0 > \alpha_1 > 0$, and φ_i is the rotational deviation of the phenyl groups from the lowest energy state.

The coordinate transformation of Equation 2.4 from the potential planes φ_1, φ_2, φ_3 yields:

$$\varphi=\frac{1}{\sqrt{3}}\left(\varphi_1+\varphi_2+\varphi_3\right);$$

$$\varphi^{'} = \frac{1}{\sqrt{6}} \left(2\varphi_1 + \varphi_2 + \varphi_3\right);$$

$$\varphi^{''} = \frac{1}{\sqrt{2}} \left(\varphi_2 - \varphi_3\right). \tag{2.5}$$

By assuming that $\varphi^{'}$(t)=$\varphi^{''}$(t)=0, Equation 2.5 can be rewritten as a differential equation of molecular motion:

$$\theta\ddot{\varphi} + \chi\dot{\varphi} + \alpha\left(\varphi - \varphi_0^{'}\right) = 0$$

$$\varphi(0) = \varphi_0; \frac{d\varphi}{dt}|_{t=0} = 0 \tag{2.6}$$

where θ is the rotational inertia of the phenyl group, φ is the angular deviation from the planar state φ_0, and α is an electrostatic spring or directional moment proportional to torque which returns phenyl groups back into plane. The microfriction factor is:

$$\chi = 8\pi r^3\eta \tag{2.7}$$

where r is the radius of a phenyl group, and η is the dynamic bulk viscosity. For large values of the microfriction factor ($\chi^2 >> 4\chi\theta$), the phenyl groups return from its deflection angle φ to the planar state φ_0 in an aperiodic motion, where exponential decay dynamics is described by:

$$\varphi(t) = \delta \cdot exp\left(-\frac{1}{t^*}\right) + \varphi_0 \tag{2.8}$$

$$t^* = \frac{\chi}{\alpha}$$

where δ is the difference between the two rotation angles where the minimum energies S0 and S1 exist, and t^* is the characteristic relaxation time constant. The rate of the deactivation processes through conformational changes is given by:

$$B(\varphi) = \beta(\varphi - \varphi_0)^2 \tag{2.9}$$

where β is a proportionality constant. With the inclusion of Equation 2.9, the probability ϱ(t) that the molecule is in the excited state can be expressed by:

$$-\frac{d\varrho}{dt} = \left(\frac{1}{\tau_0} + B(\varphi)\right) \varrho(t) \tag{2.10}$$

After solving the differential equation and performing the Taylor expansion in terms of fluorescent quantum yields:

$$\phi = \frac{1}{\tau_s}\int_0^{\infty} \varrho(t)dt = \frac{\tau_0}{\tau_s}\int_0^{\infty} e^{-x-m^2-x^3}dx \tag{2.11}$$

where τ_s is the lifetime of a fluorophore in the absence of rotational relaxation, τ_0 is the natural lifetime, ϱ is the probability that the molecule is in the excited state and :

$$m = \sqrt{\frac{\beta \cdot \delta^2\tau_0^3}{3t^{*2}}} = \frac{\sigma}{\eta} \tag{2.12}$$

where σ is a dye dependant constant that contains all viscosity independent variables (α, β, δ, and τ_0). In two limiting case, one when m<<1, fluorescence dominates (i.e. in glass at 77K) and Equation 2.11 is reduced to:

$$\frac{\tau_s}{\tau_0} \cdot \phi = 1 - \frac{6 \cdot \sigma^2}{\eta^2} \tag{2.13}$$

and in the other when m>> 1, rotational relaxation dominates in normal viscous fluids, thus reducing Equation 2.11 to:

$$\frac{\tau_s}{\tau_0} \cdot \phi = 0.893 \cdot \left(\frac{\eta}{\sigma}\right)^{\frac{2}{3}}. \tag{2.14}$$

The relation between quantum yield and viscosity was confirmed experimentally by curve fitting of quantum yield for crystal violet and is known as the Förster-Hoffmann equation.If expressed in a non-logarithmic form it results in:

$$\phi = C\eta^x \tag{2.15}$$

$$C = 0.893\frac{\tau_s}{\tau_0}\sigma^{-\frac{2}{3}},$$

$$x = \frac{2}{3}.$$

and in logarithmic form:

$$log\phi = x \cdot log\eta + C \tag{2.16}$$

where ϕ is quantum yield, x is dye dependant constant, η is viscosity, and C is the proportionality constant. The graph of experimental validation of the Förster-Hoffmann equation for a fluorescent rotor DCVJ in solvents with different viscosities is shown in Figure 2.6, where slope x=0.6 [8].

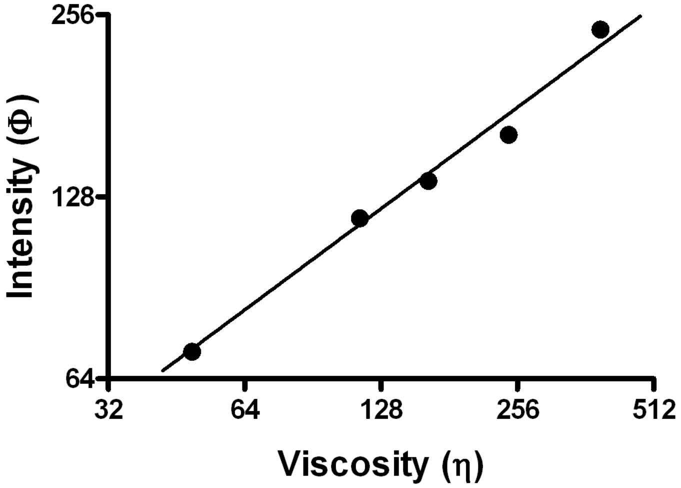

Figure 2.6: Plot of Intensity (ϕ) vs. Viscosity (η) for DCVJ in solvents with varying viscosities. Adapted from [6]

Another validation of the Förster-Hoffmann equation was done by Iwaki et al. and Haidekker et al. for molecular rotors CCVJ and DCVJ in solvents with different viscosities (split between ethylene glycol and glycerol in varying ratios), with quantum yield highest in glycerol and lowest in ethylene glycol, and in midway for glycerol:ethylene glycol mixture (Figure 2.7) because ethylene glycol and glycerol have similar polarity [7, 8].

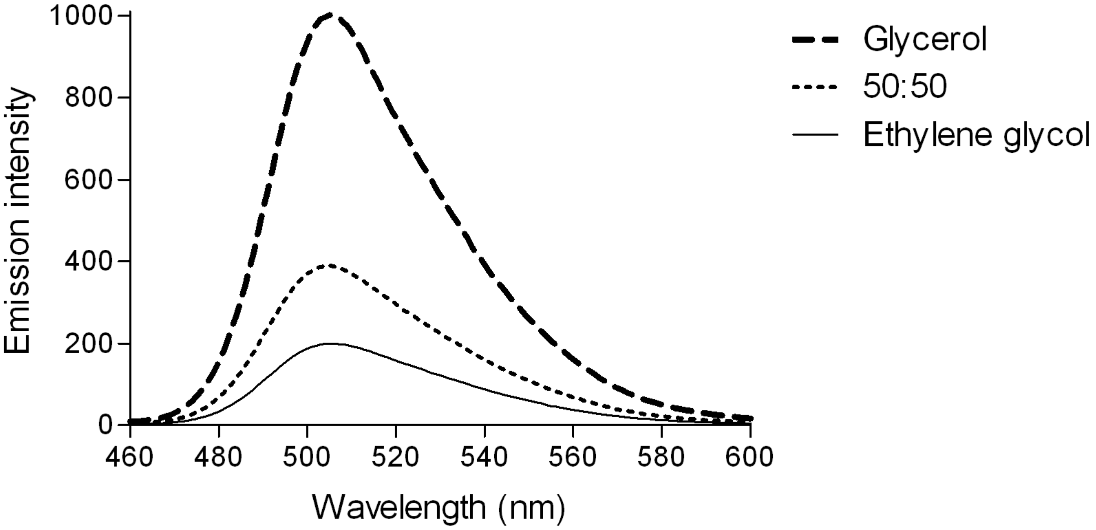

Figure 2.7: DCVJ emission spectra in viscous solvents: glycerol, 50:50 glycerol:ethylene glycol, ethylene glycol(highest to lowest viscosity). Adapted from [7, 8].

An alternative derivation of relation between quantum yield and viscosity in terms of free volume was done by Loutfy et al, resulting in the same logarithm relation shown in Equation 2.16. They defined quantum yield from Equation 2.15 in terms of radiation and nonradiative rate constant:

$$\phi_f = \frac{k_r}{k_r + k_{nr}} \tag{2.17}$$

In their natural state, molecular rotors predominantly undergo intramolecular rotation, thus having a low quantum yield in contrast to the high quantum yield of photon emission in viscous solvents. By taking this into account, Equation 2.17 can be modified if $k_{nr} >> k_r$,

$$\phi_f = \frac{k_r}{k_{nr}} \tag{2.18}$$

The application of the WLF model for temperature dependance of viscosity reinforced the idea of using free volume when describing the rotation independent non-radiative decay rate:

$$k_{nr} = k^{\circ}_{nr} e^{-\frac{xV_o}{v_f}} \tag{2.19}$$

where k°_{nr} is the free rotor reorientation rate. The intramolecular rotation in molecular rotors is limited by the free volume of the solvent, and is sterically hindered in solvents with low free volume. Any variation can be decribed in terms of free volume with:

$$\eta = A \cdot e^{\left(B\frac{V_0}{V_f}\right)} \tag{2.20}$$

where η is viscosity, A and B are constants for a single substance, $\frac{V_0}{V_f}$ is the relative free volume for a single substance at fixed pressure [30, 31].

The non-radiative decay rate can be written in terms of quantum yield:

$$k_{nr} = k_r \left(\frac{1}{\phi - 1}\right) \tag{2.21}$$

and after substitution into Equation 2.19, yields [32].

$$\phi = \frac{k_{nr}}{k^{\circ}_{nr}} e^{\frac{xV_o}{V_f}} \tag{2.22}$$

The expression for orientational relaxation time $\tau_{or} = C\left(\frac{\eta}{T}\right)$ can be expressed in terms of quantum yield:

$$\tau_{or} = \tau_r \left(\frac{\phi}{\phi_o - \phi}\right) \tag{2.23}$$

where ϕ_o is the limiting fluorescence quantum yield measured when internal dye rotation ceases, and τ_r is the radiative lifetime of the excited state.

If $\phi << \phi_o$, Equation 2.23 can be simplified to:

$$\phi = \phi_o \left(\frac{C}{\tau}\right)\left(\frac{\eta}{T}\right) \tag{2.24}$$

where C is geometry dependent friction coefficient.

By combining the term for orientational relaxation time (Equation 2.23) and Equations 2.19 and 2.22, the torsional relaxation rate k$_{or}$ can be expressed.

$$k_{or}\left(\frac{\eta}{T}\right) = A + B\left(\frac{\eta}{T}\right)^{1-x} \tag{2.25}$$

where the quantity $k_{or} * \left(\frac{\eta}{T}\right)$ should be independent of solvent viscosity if Debye-Stokes-Einstein (DSE) hydrodynamic model is operative (diffusive effects slow down the bond twisting), and if free volume is a controlling factor $k_{or} * \left(\frac{\eta}{T}\right)$ depends on $\left(\frac{\eta}{T}\right)^{1-x}$. By combining Equations 2.20, 2.22, expression for quantum yield and its dependance on viscosity can be derived:

$$\phi = B\left(\frac{\eta}{T}\right)^{x} \tag{2.26}$$

where B=$\left(\frac{k_r}{k_{nr}^0}\right)\left(\frac{T}{A}\right)^x$ [32]. Furthermore, by taking logarithms of Equations 2.20 and 2.22, quantum yield be expressed as:

$$log\phi = a \cdot log\eta + C \tag{2.27}$$

which corresponds to the Förster-Hoffmann Equation [33].

In 1983, Förster and Hoffmann's findings were complemented by those of Grinvald et al. who performed time-resolved fluorescent techniques on voltage sensitive dyes, and found that the ability to undergo intramolecular rotation and electron exchange between the electron donor and electron acceptor group are central to the understanding of dyes in viscous solvents [34]. Further expanding on this topic, it has been shown that in high viscosity solvents as glycerol (934 mPa·s), the TPM dyes approached quantum yield saturation at high temperatures, thus displaying fluorescence quenching, which in turn limits the intramolecular rotation [35].

At low molecular rotor concentrations, the concentration linearly increases emission intensity I_{em}, and if absorbed light I_{ab} intensity can be deduced , then the emission intensity is directly proportional to quantum yield:

$$I_{em} \propto I_{ab}\phi \tag{2.28}$$

The constant C can be determined, but it's often impractical, therefore under the assumption of constant absorption, constant temperature, and relatively small background light, thus eliminating the constant C, the relative changes of the solvent viscosity can be calculated by measuring emission intensities I_1 and I_2, which correspond to viscosities η_1 and η_2:

$$\frac{\eta_1}{\eta_2} = \left(\frac{\phi_1}{\phi_2}\right)^{\frac{1}{x}} = \left(\frac{I_1}{I_2}\right)^{\frac{1}{x}} \tag{2.29}$$

Intensity of one solvent can be measured from its viscosity and Equation 2.28 can be used to solve another solvent's viscosity. This method is particularly useful for instrument calibrations of familiar fluids [36].

Additionally the fluorescence lifetime (time during which a molecule is in an excited state before it returns to the ground state) was calculated for fluorescent dyes in viscous solvents:

$$\frac{1}{\tau} = k_f + k_{nf} \tag{2.30}$$

where τ is fluorescence lifetime, k_f is the intrinsic radiation rate constant, and k_{nf} is the non-radiative rate constant. The lifetimes can be used to decribed quantum yield (Equation 2.23) and therefore strongly depend on viscosity and due to vacancy of noncovalent bonds don't depend on any other property. In rigid environments, lifetime is in the order of nanoseconds, while in methanol at room it's several picoseconds all molecular rotors [29].

The utilization of molecular rotors faces similar obstacles as those of many other quantative fluorescent methods. The measurement of quantum yield for molecular rotors with lifetime systems below 1 ns with lifetime fluorophotometers is expensive and rarely used.

Consequently, it is more feasible to measure steady-state fluorescence under constant illumination, however the limitations of relative viscosity measurement need to be taken into account, since quantum yield influences the steady-state emission intensity.

Some additional factors influencing the measurement of viscosity from quantum yield, such as the absorption of emission or excitation by the solvent, and the scattering of small particles in turbid fluids by the light, need to be taken into account. By measuring the fluid's absorbance at the dye's excitation wavelength, the dye concentration can be accounted for:

$$\eta = \xi \cdot I_{em}^{k} \tag{2.31}$$

where ξ is a proportionality constant of corrected factors, I_{em} is the measured intensity, and k is inverse of the dye dependant constant.

Chapter 3

Contemporary Usage of Molecular Rotors

3.1 Electrochromic Fluorescent Probes

A subgroup of cyanine dyes, styryl dyes (general chemical structure shown in Figure 3.1) provide a relatively large emission intensity and can be used as electrochromic (voltage sensitive) fluorescent probes to measure responses from various cell cultures. Grinvald et al, successfuly applied this technique as an alternative to microelectrodes to measure active and passive electrical properties, especially in membranes, which until then had been cumbersome, technically difficult or impossible, while with electrochromic dyes it's possible to obtain measurements with high spatial resolution and sampling frequency [9].

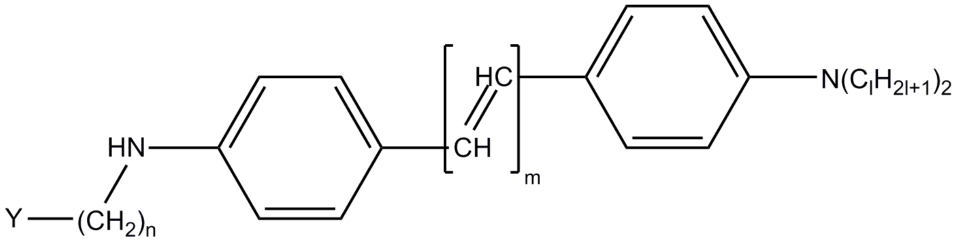

Figure 3.1: General chemical structure of synthesized styryl dyes. Y=SO_{3-}, PO_{3-}, $(Et)_3N^+$, $(Me)_3N^+$; n=3,4,5, CH_2-ϕ; m=1,2; l=1,2,3,4; λ^*_{max}=500-572 nm (peak emission in absolute ethanol). Adapted from [9].

Conventional electrical recording techniques had been limited by the number of microelectrodes that can be inserted into the tissue, and intracellular recording can only be made for large cell bodies, not small dendrites and axons [37].

Active transport processes have certain ion (potassium, sodium, and chloride) concentration gradients which result in the cell plasma membrane of $\approx$ -70 mV. Changes in the membrane potential (hyperpolarization and depolarization) is an important property of a wide array of biological systems and processes, some of them including an information transfer in neuronal networks, muscle contraction, and energy transduction during photosynthesis and metabolism. Nonetheless, due to the small size of membranes (typically in nanometers), it's almost technically impossible to accurately measure any changes in membrane potentials.

The testing was done on a dissected segmental invertebrate ganglia from leeches, rat mammalian neurons, and mouse neuroblastome cells. The rat hippocampus slice preparation expedited the study of neuronal interactions because it allows prolonged intracellular recording and the control of cellular environment, while a photodiode array detected fluorescent signals of action potential measurement in a 2μm wide neuronal process.

The results demonstrated an exceptional sensitivity of the fluorescence recording technique with styryl dyes, therefore becoming a tool to study large nerve processes or growth cones, the recording of electrical activity and synaptic responses of the synapses within a neuropil in disassociated cell cultures, and intact central nervous system preparations when the dye is iontophoretically (introduction of an ionized substance by the application of a direct electric current) injected into single cells [34].

3.2 Microviscosity Measurement With Fluorescent Imaging

Styrylpyridinium dyes change their fluorescent properties following changes in electronic structure as a feedback to variations in the electric field. In excitable cells, their feedback allows them to detect changes in membrane potential on the millisecond scale, however, their potential dependant quantum yield change is about 2-10% per 100mV.

A derivative of styryl dyes, DMASP (4-[4-(dimethylamino)styryl]pyridine), demonstrated a wavelength ratiometric response to viscosity. In aqueous solutions, DMASP is highly soluble and strongly fluoresces, with dual excitation peaks at 360 and 469 nm, and the mission range of 500 to 650 nm. With increasing polarity likely due to an intramolecular $\pi^* - \pi$ charge transfer transition, a DMASP derivative with the long absorption wavelength move to lower energies, and the quantum yield emission spectra in the excited state showed sensitivity to solvent polarity.

An N-carbonmethyl butyl ester DMASP was successfully inserted into a living smooth muscle cell, and after crossing the cell membrane was hydrolyzed by cellular esterases, a group of enzyme which catalyzed the hydrolysis of esters, and transformed it into a membrane-impermeable fluorescent carboxylate DMASP derivative (Figure 3.2).

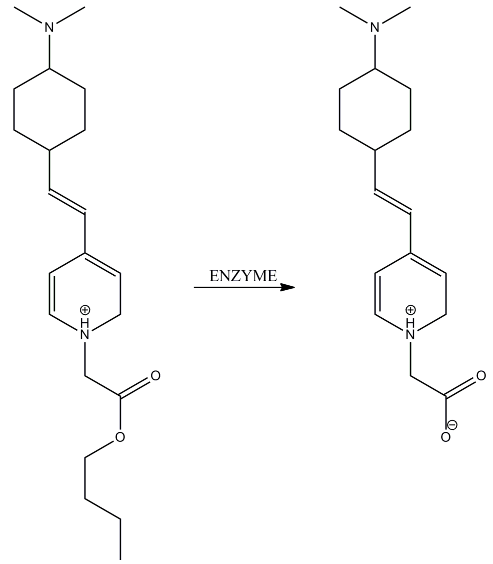

Figure 3.2: Chemical structures of N-carbonmethyl butyl ester DMASP in its extracellular (left) and intracellular form (right). Adapted from [10].

The cytoplasm viscosity of that cell was obtained with fluorescence imaging microscopy, with a spectrofluorimeter in dual-excitation single emission mode. The calibration against viscosities of glycerol/water and sucrose/water mixtures provided viscosity from the quantum of smooth muscle cells, and it closely matched the literature values, thus proving it's possible to follow minute changes of quantum yield and microviscosities [38, 10, 39].

3.3 Molecular Rotors and Fluorescence Lifetime Imaging

Viscosity changes in various biosystems have been linked to diseases and defects in cells. These problems are caused by the movement of chemicals within cells, which affects signaling, transport and other processes, however imaging microviscosity in cells is very difficult, and fluorescence based intensity measurements posses problems in molecular rotor calibration. Also, it can be changed by fluctations in the fluorescent dye concentrations, and inhomogeneities in the optical properties of the medium and viscosity. This technique could possibly be improved with the use of fluorescent dyes with two chromophores, which could absorb cetain light wavelengths, where one chromophore would behave as a molecular rotor, and the other one would be insensitive to viscosity but can be used to measure concentration. Nevertheless, it's been experimentally demonstrated that fluorescence lifetime imaging (FLIM) can be used to overcome any difficulties with obtained data the other techniques have [11].

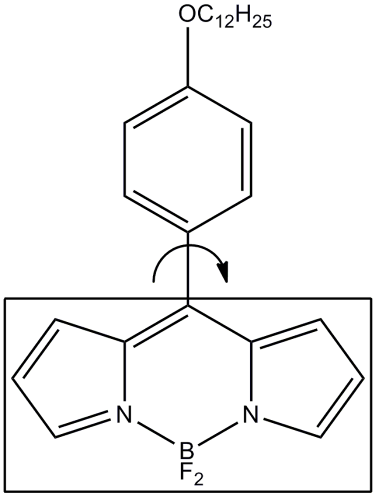

Figure 3.3: Chemical structure of 4,4'-difluoro-4-bora-3a,4a,-diaza-s-indacene. The core BODIPY fluorophore is contained within the rectangle. Addition of substitutients to the core molecule can shift the emission spectra towards higher wavelengths. Arrow denotes the rotation axis. Adapted from [11].

A subgroup of molecular rotors, BODIPY dyes, were used by Kuimova et al. BODIPY dyes can be used to generate fluorescent conjugated of nucleotides, enzymes, fatty acids and polystyrene microspheres.They are relatively nonpolar and the chromophore is electrically neutral. Different types of BODIPY dyes consist of water soluble esters, fluorescein substitutes, and amine reactive dyes.

Fluorescence measurements were made in methanol/glycerol mixture containing a molecular rotor (Figure 3.3) and other derivatives, and an increase in quantum yield was seen with increasing solvent viscosity. The phenyl group rotation was restricted in high viscosity solvents, and the non-radiative decay constant k'_{nf} increased with decreasing viscosity while the radiative decay constant k'_f remained constant. Measured lifetimes for a molecular rotor in Figure 3.3 are larger than 100 picoseconds, which is the range of detected by time correlated single photon counting, thus offering ultrasensitive lifetime detection [11].

3.4 Molecular Rotors and Nucleotides

The most popular and versatile tools for the measurement of intracellular concentration of different ions and other messengers involved in the transduction of biological signals are fluorescent indicators. Fluorescence can be used to whole cells with high spatial and temporal resolution while cells undergo physiological responses [40].

A type of fluorescent indicators, EDAs (Electron Donor-Acceptor molecules) are used as chemosensors for ions, micelles, and polymeric matrices because they display fluorescence from ICT (intramolecular charge transfer) states, but not from TICT states. Therefore a dye was synthesized that posseses the photophysical properties of EDAs and and charge transfer mechanism of TICT states.

When the dye (trans-4-(p-N,N-dimethylaminostyryl)-N-vinylbenzylpyridinium chloride) was photoexcited, it had a large dipole moment of about 18D between ground and excited states in both polar protic and polar aprotic solvents, which resulted in a strong solvatochromic behavior. The resulting large dipole moment was due to formation of the TICT states and the electron transfer from the dimethylamino donor group to the vinylpyridinium acceptor group.

The dye was used is association with negatively charged nucleotides cAMP, cGMP, and purine and pyrimidine nucleotides. In the presence of cAMP, the quantum yield of the dye increased 12 fold, but in CMP and UMP, which are pyrimidine nucleotides, there was no change in quantum yield. cGMP exhibited a similar quantum yield increase to that of cAMP, but in AMP, APP, ATP (purine nucleotides) and adenosine, the quantum yield increase was much smaller.

Changes of quantum yield occured only with dye being present in nucleotides with a purine base which enhanced the TICT mechanism of the dye, and are improved by ribose and phosphate moieties, but pyrimidine nucleotides showed no effect on quantum yield. Since the styryl pyridinium dye derivative preferentially associated with cAMP and cGMP, it could possibly be used to prepare fluorescently imprinted polymer chemosensors due to the presence of a vinyl group [41].

3.5 Molecular Rotors and Phospholipid Bilayer Viscosity

Fluorescence Recovery After Photobleaching (FRAP) and fluorescence anisotropy are two well established methods to measure membrane viscosity [42, 1]. FRAP measures diffusivity of specific membrane bound fluorescent dye, and fluorescence anisotropy measures depolarization of fluorophores excited by polarized light, where mebrane depolarization depends on membrane fludity. An alternative approach to meausure membrane viscosity is to use molecular rotors, more specifically for this study it's FCVJ ((2-carboxy-2-cyanovinyl)-julolidine farnesyl ester), chemical structure is shown in Figure 3.4.

Nipper et al examined the quantum yield of FCVJ in liposome model membraned during periods of exposure to viscosity altering substances. Substances such as alcohols reduce viscosity, where size of the hydrocarbon chain is approximatelly proportional to the observed viscosity decrease, while cholesterol tends to increase viscosity. Short chain alcohols localize predominantly at the hydrophilic group of the phospholipid bilayer, and this particular

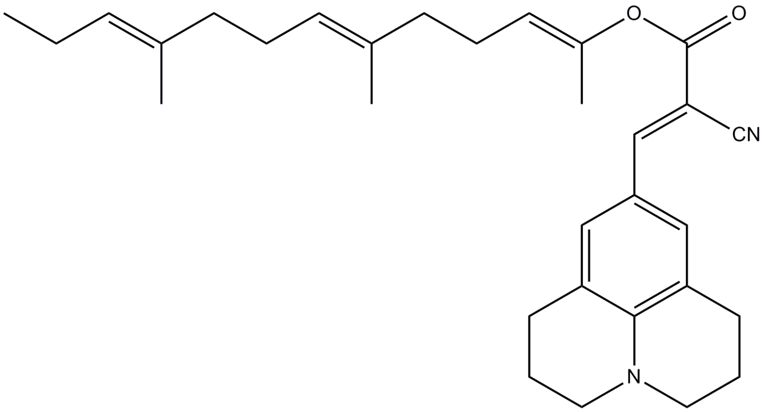

Figure 3.4: Chemical structure of (2-carboxy-2-cyanovinyl)-julolidine farnesyl ester

location alters the natural microstructure of the lipid membrane, which leads to viscosity decrease.

Alcohol concentration increases the density of the alcohol at the phospholipid surface, and this was proved with FCVJ and an increasing propanol concentration which led to viscosity decrease. Organic solvents, DMSO and cyclohexanes produced a reduction in mean quantum yield of FCVJ in FCVJ stained liposomes, thus indicating viscosity decrease, while quantum yield of FCVJ in the presence of cholesterol and nimesulide exhibited an opposite effect of an increasing viscosity. A backcalculated viscosity from FRAP was compared to viscosity values from FCVJ stained liposomes, and the correlation value was found to be very high [27].

In another study by Sawada et al, molecular rotors with hydrophilic groups were integrated into a rabbit skeletal muscle, where the G-F transformation of actin was observed. The results showed that the solvent viscosity dependent fluorescence was greater in F-actin [43]. Furuno et al. used a confocal fluorescence microscope to examine the exocytitic secretory processes of rate mast cells with DCVJ. Quantum yield of DCVJ increased in the cytoplasm, suggesting that DCVJ bound itself to the proteins in the cytoplasm [44].

CHAPTER 4

VISCOSITY, FLOW AND SHEAR STRESS, FLOW MEASUREMENT

4.1 VISCOSITY, FLOW AND SHEAR STRESS

Most substances deform under shear stress, and more specifically in fluids, this property to resist deformation is called viscosity. The relation between viscosity and shear stress can be expressed with:

$$\mu = \frac{\tau}{\frac{dx}{dy}} \tag{4.1}$$

where μ is dynamic viscosity, τ is shear stress, and $\frac{dx}{dy}$ is the gradient of velocity of fluid between parallel layers shown in Figure 4.1. Dynamic viscosity involves force, while the viscosity that doesn't involve force is called the kinematic viscosity and can be represented with:

$$\nu = \frac{\mu}{\rho} \tag{4.2}$$

where ρ is density.

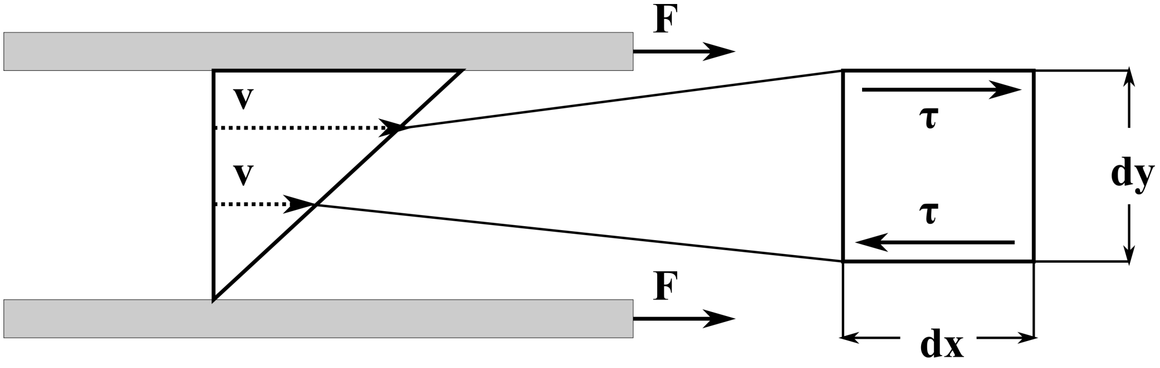

Figure 4.1: Profile of constant velocity and shear stress acting on a fluid between two layers

Non-Newtonian fluids used in this study have constant viscosity, while in Newtonian fluids viscosity changes following an increase/decrease in temperature. This results from the relatively high cohesion (attraction) of molecules. Solids and fluids can be differentiated by their properties in relation to their resistance to shear stress (Figure 4.2). The ideal fluid has no viscosity and is represented with a horizontal line, the elastic solid is represented with a vertical, and in Newtonian fluids viscosity doesn't change with shear stress [12, 45].

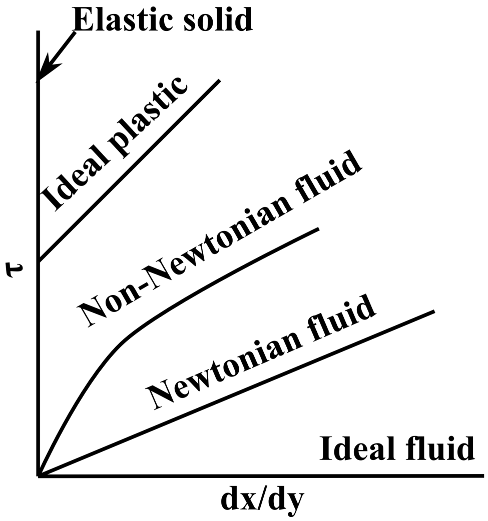

Figure 4.2: Shear stress vs. Gradient for different substances. Adapted from [12]

4.2 Flow Measurement

4.2.1 Doppler Ultrasound

As a noninvasive imaging tool, Doppler Ultrasound uses the Doppler effect to image internal organs and blood flow in real time by utilizing high frequency sound waves, most often in the range of 1-20 MHz. The Doppler effect relates the transducer frequency to the perceived frequency by:

$$f_p = f_D \cdot \left(\frac{v \pm v_0}{v \pm v_s}\right) \tag{4.3}$$

where f_p is the perceived frequency, f_D is the transducer frequency, v is the wave velocity, v_0 is the observer velocity, and v_s is the source velocity. Sound waves emitted by a transducer penetrate the tissue, and when the matter density varies across different layers, sound waves are reflected and scattered back to the transducer, amplified and displayed on a screen. The relatively high frequency range is manipulated as needed, depending on the tissue depth, with high frequencies having low penetration and low frequencies having high penetration power. The spatial resolution improves with low frequencies but restricts the penetration depth to a few hundred micrometers, while tissues containing too many fatty acid chains further complicate the image quality. Furthermore, the imaging and analysis of fluids such as blood restricts its use only to large vessels due to poor image quality [46].

4.2.2 MRI

MRI (Magnetic Resonance Imaging) is a contemporary noninvasive technique, primarily used to image soft tissue(s) and metabolic changes within. This process is accomplished by utilizing a range of various magnetic fields and comparing its oscillatory frequency with the frequency of the nuclei of the tissue being imaged. By introducing a magnetic field across a tissue, the Larmor frequencies vary with respect to space, and can be spatially resolved to provide more information [47]. Fourier analysis of proton nuclei precession angles produces fluid velocity vector components.[48]

Blood flow imaging done in blood vessels is restricted by vessel radius and flow geometry. Due to different types of flow (pulsatile in arteries and relatively steady in capillaries) and flow velocities, signal produced by a magnetic field is inhomogeneous, and its intensity decreases as flow velocity increases [49].

4.2.3 PARTICLE TRACKING

Methods to observe trajectories of particle motion in fluidics on a micrometer scale have been developed in response to dificulties of modeling and simulating flow with numerical applications, and especially in dealing with fluid properties, such as viscosity, density, velocity, and others.

Most widely used methods are (Micron) Particle Image Velocimetry, Scalar Image Velocimetry, and Laser Doppler Velocimetry. Particle Image Velocimetry uses flow tracing particles and has limited velocity accuracy because of the small probe volume, Laser Doppler Velocimetry uses reflected light to calculate tissue velocity and has resolution dictated by the diffraction of the optical recording system while Scalar Image Velocimetry uses molecular tracers which limit its spatial resolution [50].

4.2.4 Thermal Flowmeters

Thermal flowmeters measure the properties of a fluid flowing in a tube. This is accomplished with a heat sensor which dissipated heat to the surrounding fluid in motion. The amount of heat lost to the fluid allows the electronic reveiver to determine fluid properties from temperature readings. The accuracy of this method is constrained by its sensor sensitivity and calibration problems [51].

CHAPTER 5

SHEAR STRESS SENSITIVITY

The motivation behind this experiments was to establish shear sensitivity of CCVJ and Diol in viscous solvents. The experimental protocol included low speed shearing of molecular rotors' respective viscous solutions in a fluoroscopic cuvette, while the intensity of their emission spectra was recorded. The results provided qualitative support of this particular property for these two molecular rotors.

5.1 MATERIALS AND METHODS

A solution of 10 μM molecular rotor in fluorescence-grade ethylene glycol ($C_2H_6O_2$) was placed in a fluoroscopic cuvette, and a stir bar was introduced.In a fluorophotometer (Fluromax 3 Jobin-Yvon), emission spectra from 450 nm to 550 nm were acquired with an excitation wavelength of 422 nm for CCVJ and 434 nm for Diol. Spectra with the stirrer turned off (no shear) and with the stirrer at a low setting (moderate shear without turbulence or vortex formation, setting 3 out of 10) were acquired and compared.

5.2 RESULTS

When a viscous solution of CCVJ in ethylene glycol and viscous solution of Diol in ethylene glycol was stirred at a low speed emission intensity increased by about 15 % for CCVJ (Figure 5.1) and about 6 % for Diol (Figure 5.2) without any shift in peak wavelength.

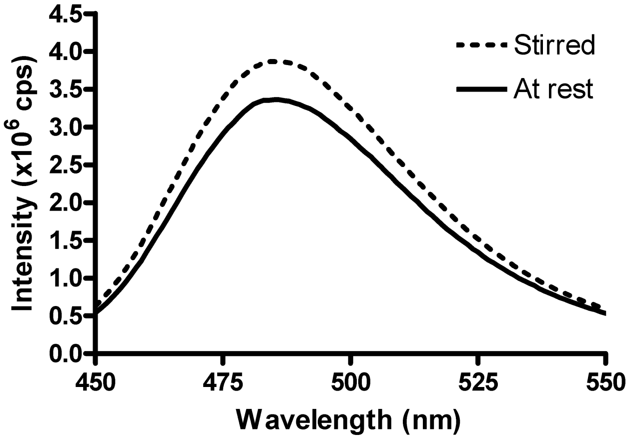

Figure 5.1: 10 μM CCVJ in Ethylene Glycol with and without stirring

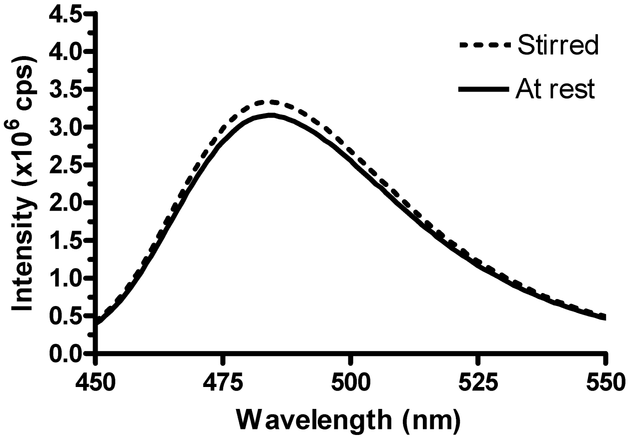

Figure 5.2: 10 μM Diol in Ethylene Glycol with and without stirring

5.3 Conclusions

This basic experiment qualitatively demonstrated shear sensitivity of molecular rotors CCVJ and Diol in a viscous solvent. This is consistent with findings of Haidekker et al.

which found that molecular containing functional groups (COOH functional group in CCVJ and triethylene glycol functional group in CCVJ-TEG) exhibited a statistically significant quantum yield increase while undergoing shearing (~20% for CCVJ and ~7% for CCVJ-TEG) [52]. In both cases, the peak wavelength didn't change, and wasn't accompanied with shear thinning.

For control experiments, a molecular rotor DCVJ , which doesn't have a polar group, and a known fluorophore fluorescein, which isn't a molecular rotor, were sheared, and no quantum yield increase was manifested. Same observations were observed for non-polar solvents such as hexanes.

We hypothesize mechanism for this behavior of water soluble molecular rotors CCVJ and CCVJ-TEG and viscous solvents depends on the property of their respective polar functional groups to form interaction with the solvent, and this entire interaction process takes place during the molecular rotor photoexcitation, before their return to the ground state.

Chapter 6

Flow Chambers

The objective behind this experiment was to examine the behavior of molecular rotors which undergo TICT state formation and non-radiative decay in viscous solvents. Viscous solutions of molecular rotors were injected in various geometries at different flow rates, while being photoexcited with a light source. The data was analyzed with a custom imaging software, and the results show a promising method to visualize flow patterns with molecular rotors.

6.1 Materials And Methods

6.1.1 Chamber Construction And Apparatus

Flow chambers (geometries shown in Figure 6.1) were constructed from polymers with thermoelastic properties, namely polycarbonate, and polyoxymethylene (commercical name Delrin). These polymers are relatively strong, and have good chemical and temperature resistance. After desired chamber grooves were milled in, a thin coating of silicone glue was applied to the inner edges of the channel(s), and Gorilla glue to the outer areas. The application of silicone glue was done to avoid any contact of solvent with the Gorilla glue, because when in contact a solidifying reaction occurs. Dimensions of a flow chamber were 8.4x4.4 cm , while the channel depth was 0.3 cm. The flow imaging apparatus is shown in Figure 6.2.

The imaging apparatus consisted of a digital, consumer-grade SLR Camera (Konica Minolta Dynax 7D Maxxum 7D equipped with a with a Sigma 50 mm f/2.8 fixed-focus lens), a D450/40 image grade emission bandpass filter (Chroma Technology Corp.), two collimated high-power LED excitation sources (Luxeon) with a center wavelength of 450 nm, two posts for the flow chamber, and one post each for the SLR Camera and emission filter. The LED sources provided broad illumination to cover the entire front side of a flow chamber. LED excitation source were connected to a custom LED driver, and provided either homogeneous light or intensity modulated light. The bandwidth of the source was reduced by excitation filters. An emission filter in the optical path blocked the excitation light and allowed only the fluorescence emission to pass.

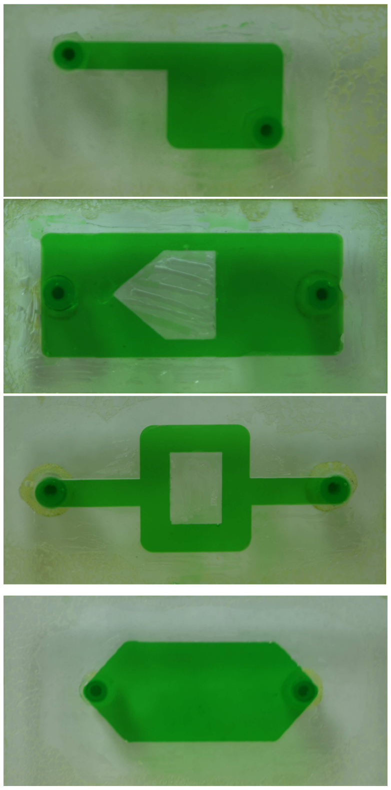

Figure 6.1: Flow Chamber Geometries: Cleaver, Pentaisland, Island, Hexagonal (top to bottom)

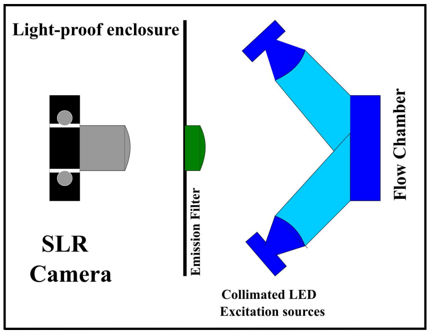

Figure 6.2: Top View Of The Imaging Apparatus

6.1.2 Camera Calibration

Since the camera is a consumer grade SLR, experiments needed to be performed to establish sensitivity, precision and repeatibility.

ISO function in cameras regulates the light sensitivity of the camera's image sensor. For the digital camera used in this study ISO settings values ranged from 100-1600. The lower the ISO setting, the lower the light sensitivity of the image sensor, making it suitable for bright scenes while the higher ISO settings are more suitable for darker images. Since noise increases with higher ISO settings, experiments were performed to find an optimal ISO setting that balances sensitivity and noise.

Average intensity in a selected object area was monitored at ISO settings from 100 to 800. Every time an ISO setting was doubled, exposure time was halved. The results shown in Figure 6.3 points to an increased sensitivity for settings below 200, and decreased sensitivity for settings above 400. while the range between 200 and 400 was constant.

An object was repeatibly exposed at ISO 100 and ISO 200 settings over a range of 10 frames. The results in Figure 6.4 and Table 6.1 show very small deviation and coefficients of variation below 1 %, and therefore good stability of exposure at those ISO settings. A similar analysis was performed to examine the stability of blue and green channel stability as a function of LED generator. The results are shown in Figure 6.5 and Table 6.2, where the coefficient of variation is below 1 %, thus proving that the light source provides is almost contant and very stable.

To examine sensitivities of the camera's red, blue and green channels, the camera without the lens was positioned in front of the fluorospectrometer light beam which was directed at the center of the charge coupled device (CCD) sensor, which is a semiconductor responsible for collecting images. The projected Gaussian spot intensity was recorded over a wavelength range from 340 to 720 nm in 10 nm increments. The Gaussian spot peak intensity was normalized by dividing it with the reference signal from the fluorospectrometer, and the resulting data is shown in Figure 6.6.

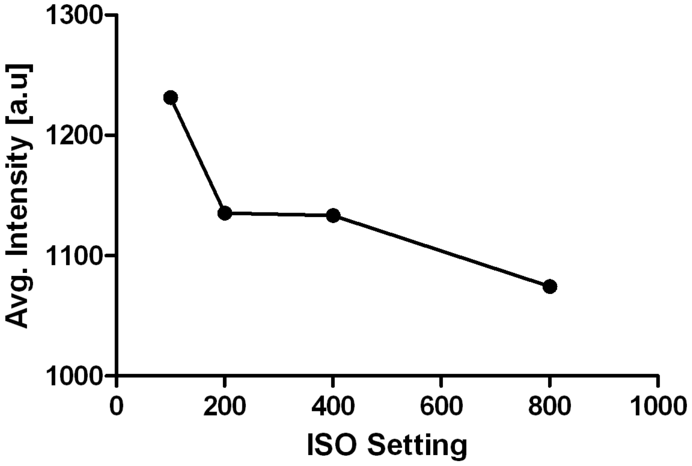

Figure 6.3: Relative sensitivity of the camera at different ISO settings determined by photographing a homogeneously gray area and keeping the product of ISO and exposure time constant.

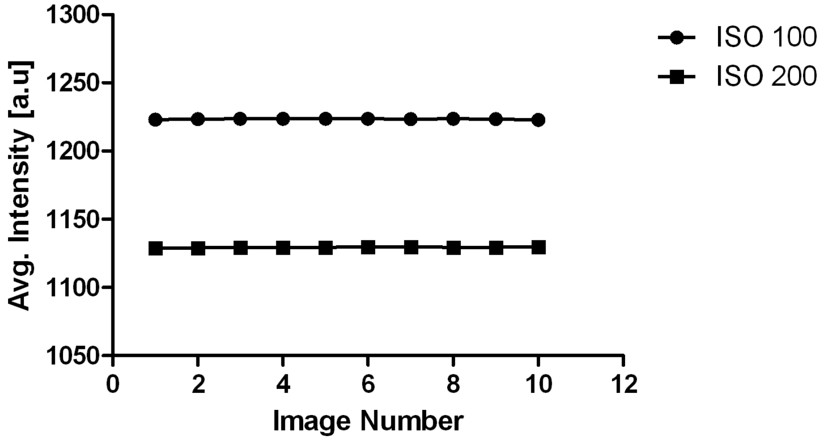

Figure 6.4: Repeatibility of the exposure at two different ISO settings. The same object was repeatibly exposed and average intensity displayed over the frame number.

Table 6.1: Average intensity variations for ISO 100 and ISO 200 settings shown in Figure 6.4

	ISO 100	ISO 200
Average Intensity	1222.9910	1129.3255
Standard Deviation	0.189505	0.699329
Coefficient of Variation	0.000155	0.000619

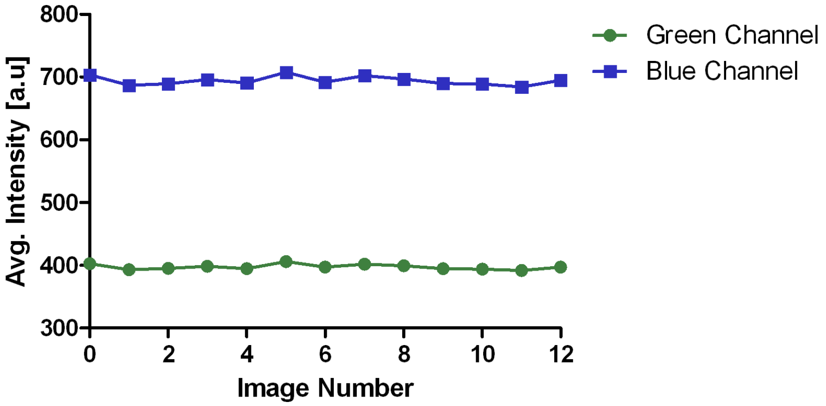

Figure 6.5: Repeatibility of green and blue channel values at a given ISO setting as a function of LED generator. The same object was repeatibly exposed and average intensity for blue and green channel displayed over frame number.

Table 6.2: Average LED intensity variations for blue and green channel shown in Figure 6.5

	Green Channel	Blue Channel
Average Intensity	400.09	699.05
Standard Deviation	3.790092	6.293250
Coefficient of Variation	0.009473	0.009003

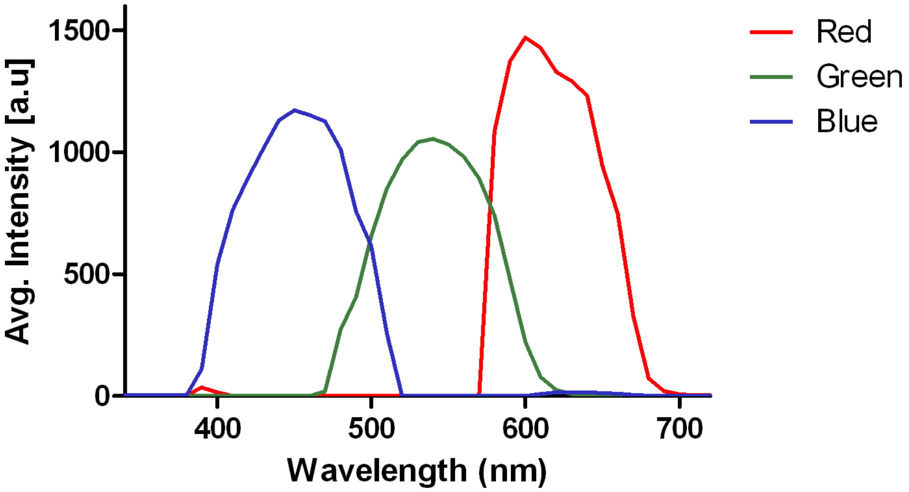

Figure 6.6: Normalized sensitivity of the camera's red, blue, and green channel. Fluorospectrometer light beam projected a Gaussian spot on the CCD sensor. Peak signal values were captured as a function of wavelength, and normalized by dividing with the reference signal.

6.1.3 Preparing And Injecting A Viscous Molecular Rotor Solution

A solution was made from 60 μl of 10μM molecular rotor stock solution in 40 ml of fluorescence-grade ethylene glycol, a solvent with viscosity of approximately 14 m·Pas. The solution of a molecular rotor in ethylene glycol was thoroughly mixed and filled into a 30 ml syringe. Syringe was then positioned in a custom syringe pump to provide precise and controllable flow rates.

6.1.4 Image Acquisition

Images were acquired with an exposure time of 8 seconds and lens aperture of f/2.8. The camera sensitivity was set to ISO 200. The camera was set to acquire RAW-format images to make use of the full 12-bit per pixel dynamic range. One set of images was taken each at 0.25, 0.50, 0.75, 1.00, and 1.50 ml/min flow rate. For each flow rate, two images with flow and two images without flow (at rest) were taken. No-flow images were intended for background intensity normalization.

After each experiment, all images were transferred to a computer for image analysis. Image processing tools were a) UFRaw, a tool to convert the RAW image format to 12 bit-per-pixel TIFF images, and b) Crystal Image (quantative image analysis software), all software running on Ubuntu Linux version 7.04. In preparation for image processing, the blue channel at peak sensitivity wavelength of 450 nm was extracted from the color image file and stored as a single-channel grayscale image for further analysis.

6.1.5 Image Analysis

Crystal Image, a quantative biomedical imaging analysis software, was used for all image analysis steps. These consisted of a) a rank filter applied to each image individually to reduce noise, b) computation of a normalized difference image by using the following equation embedded in a computer macro:

$$I(x,y) = \frac{(I_{F1} + I_{F2}) - (I_{NF1} + I_{NF2})}{(I_{NF1} + I_{NF2})} \tag{6.1}$$

where I_{F1} and I_{F2} represent the two flow images, and I_{NF1} and I_{NF2} represent the two no flow images.

By creating the normalized image difference any background inhomogeneities were removed. After using the two images added together, signal to noise ratio was increased by about 40 %. The resulting normalized image was c) further denoised with either Gaussian smoothing filter or Anisotropic diffusion filter and d) false-colored to enhance visual perception of contrast. Anisotropic diffusion filter can be derived from Gaussian smoothing. Unlike Gaussian smoothing, Anisotropic diffusion incorporates a factor which enables it to preserve information contained in the edges, while reducing the noise [53].

6.1.6 COMPUTED FLUID DYNAMICS

For the Computed Fluid Dynamics (CFD) modeling, the open-source software NAST++ was used [54]. NAST++ is a C++ solver for the Navier-Stokes equation in three directions. Flow chamber geometries were discretized at 360 by 180 by 80 points. Entry and exit ports were modeled as circular openings with constant-flow and zero-pressure boundary conditions, respectively. All other boundary cells were set to no-slip boundary conditions.

The mathematical model used was the dimensionless time-dependent incompressible Navier-Stokes equation:

$$\frac{\delta u}{\delta t} + u \cdot \bigtriangledown u = \frac{g}{Fr} - \bigtriangledown p + \frac{1}{Re} \bigtriangleup u \tag{6.2}$$

$$x \in \Omega, 0 \leq t \leq T_{fin}$$

$$\bigtriangledown \cdot u = 0$$

with defined initial and boundary conditions where g is acceleration, Fr is the Froude number, Re is the Reynolds number, Ω is the computational domain, T_{fin} is the timespan of the simulation. Reynolds number Re describes the ratio between inertia and flow viscous forces, and can be expressed with:

$$Re = \frac{\rho L u_\infty}{\mu} \tag{6.3}$$

where μ is the dynamic viscosity, ρ is density, L is a characteristic length, and u_∞ is the characteristic velocity. The ratio of inertia and gravitational forces is called Froude number, and is defined as:

$$Fr = \frac{u_\infty^2}{L}. \tag{6.4}$$

The Prandtl number is:

$$Pr = \frac{\nu}{\alpha} \tag{6.5}$$

where ν is the kinematic viscosity and α is the heat diffusion coefficient. As an example, typical values used for the cleaver geometry were: Re=0.84, g=0, Pr=1.

After convergence, three matrices were obtained with the velocity component in x, y, and z direction. A flow magnitude field was computed using:

$$|v| = \sqrt{v_x^2 + v_y^2 + v_z^2} \tag{6.6}$$

and projected into two-dimensional space by averaging along the z-axis, which corresponds to the fluorescence imaging process. The resulting projected flow magnitude was visualized with the same method as the fluorescent images.

6.1.7 Particle Tracking

Fluorescent polystyrene microspheres for flow determination (obtained from Molecular Probes) were used to to make a 14 μM solution in 25 ml of ethylene glycol. The green fluorescent microspheres measured 15 μm in diameter with absorption and emission wavelengths at 450 nm and 480, respectively. A concentration of $1.0x10^6$ beads/ml was used. Camera settings included exposure at 8 seconds and f/2.8 apperture with an ISO setting of 800. Because of the long exposure time, the brightly fluorescent beads would show up as streaks in the image, representing streamlines.

6.2 RESULTS

Spatially resolved fluorescence intensity images were acquired in four different geometries, and for all of them , the overall intensity increased with an increase in the flow rate (Figures 6.9, 6.11, 6.15, 6.19), while in the geometries with narrow channels and higher flow rate, higher fluorescence intensity was observed, as opposed to the wider regions and high flow rates. For the hexagonal geometry (Figure 6.8), intensity fades from left to right (following the direction of injection), and for a region selected in the central part of the chamber, intensity decays for all flow rates (Figure 6.10).

For the flow geometry in Figure 6.11, an excellent match with flow magnitude computed with CFD simulations was found (Figure 6.13), especially the higher intensity in the narrow inflow channel caused by the higher flow rate, in contrast to the wide basin channel and the lower flow rate (Figure 6.14).

For the flow geometry in Figure 6.15, CFD simulation of flow magnitude are a little less pronounced (Figure 6.17), and as the stream splits above and below the reactangular island, a decrease of fluorescence intensity consistent with halving of the flow rate can be observed (Figure 6.18).

For the flow geometry in Figure 6.19, a moderate visual match with CFD simulated flow magnitude can be seen (Figure 6.21), and not with shear stress magnitude (Figure 6.22), where the lowest shear stress is in regions 1 and 2, but not in the mid-channel as shown in fluorescenct images.

To further examine the cause of prominent fading along the flow direction and establish the flow patterns, streamlines were acquired with fluorescent in ethylene glycol without the presence of any dyes in the hexagonal geometry. The observations point to absence of anomalities and/or irregularities in the downstream regions, and also the lack of movement of some microbeads, very likely caused by them sticking to the chamber (Figure 6.7). The no-flow (no shearing applied) images for the hexagonal and cleaver geometry are shown in Figure 6.8, and it can be observed that fluorescence is relatively homogeneously distributed without any fading over distance, thus indicating that the fading phenomena occurs only when the viscous fluid with molecular rotors is sheared.

Placing a piece of paper in front of a chamber in the mid-region, and acquiring fluorescent images afterwards (Figure 6.23), shows an intensity decay in the region to the left of the paper (slope=-0.12), a continuous intensity decay in the region covered by the paper (slope=-0.5), and an decay in the region to the right of the paper (slope=-0.08) (Figure 6.24).

By covering half of the chamber with a piece of paper (Figure 6.25), fluorescent images show that the intensity decay start immediately in the uncovered region, and not beforehand in the covered region (Figure 6.26). Any influence of photobleaching was excluded by analysing intensity change over a series of no-flow images in selected region of a flow chamber, which showed no variations.

Fluorescent intensity decay can be seen for viscous solution of CCVJ in EG, CCVJ-TEG in EG, and Diol in EG (Figure 6.27), indicating it occurs for each molecular rotor, and reversal of the flow injection didn't alter the trend (Figure 6.28). Viscous solutions of CCVJ in EG, and Diol in EG taken for flow rates ranging from 0.25 ml/min to 4 ml/min, shows an increasing trend in both cases, and for CCVJ in EG it reaches a saturation level at high flow rates, but this doesn't hold for Diol in EG (Figure 6.29). Moreover, a control experiment was performed with Lucifer Yellow (a common fluorescent dye) in ethylene glycol, and in this case the solution showed no shear sensitivity in response to increasing flow rates. Curve fitting with the empirical relation between viscosity and flow is an exponential association decribed by:

$$\Delta I = \Delta I_{max} \cdot \left(1 - exp\left(-\frac{\eta}{\eta_c}\right)\right) \cdot \left(1 - exp\left(-\frac{v}{v_c}\right)\right) \tag{6.7}$$

and can be further modified for a Newtonian fluid with constant viscosity:

$$\Delta I = \Delta I_{max} \cdot \left(1 - exp\left(-\frac{v}{v_c}\right)\right) \tag{6.8}$$

where ΔI is measured intensity, ΔI_{max} is intensity span which depends on viscosity, v is fluid velocity, and v_c is characteristic velocity. From this equation it emerges that the characteristic flow, viscosity constant and the intensity span are both solvent and molecular rotor dependent[52], provides values for constant viscosity v_c^{-1}=1.556 (R^2=0.99) for CCVJ in EG, and v_c^{-1}=0.176 (R^2=0.94) for Diol in EG. This particular equation was chosen because of good correlation values.

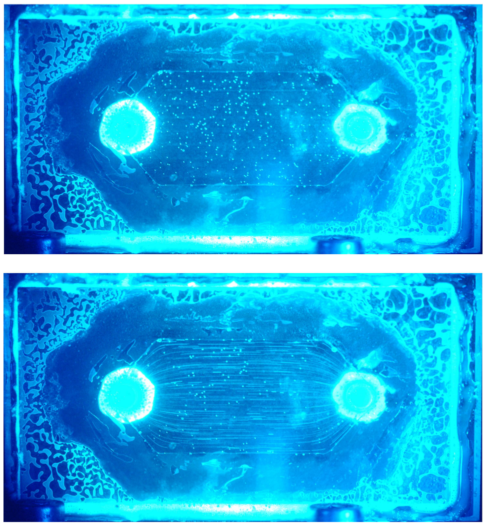

Figure 6.7: Fluorescent microbeads at rest (top), and at 1.50 ml/min (bottom)

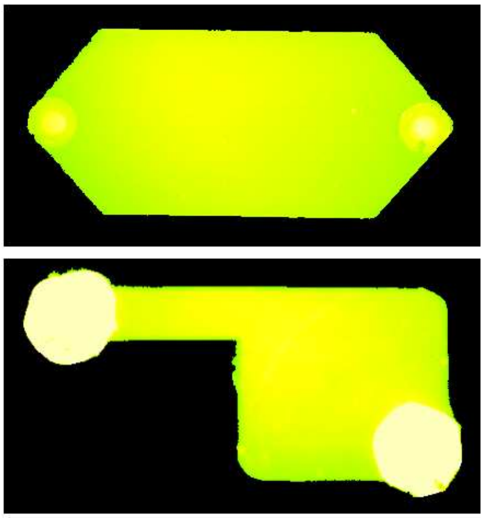

Figure 6.8: No flow images of the hexagonal geometry (top) and cleaver geometry (bottom)

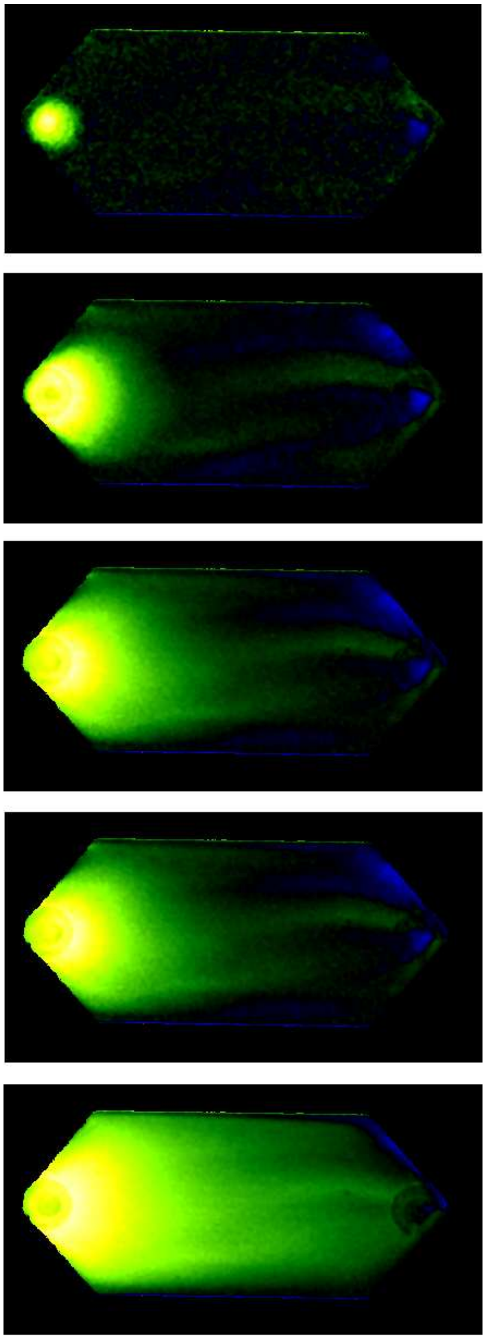

Figure 6.9: Flow images of the hexagonal chamber. Flow rates: 0.25, 0.50, 0.75, 1.00, 1.50 ml/min (top to bottom).

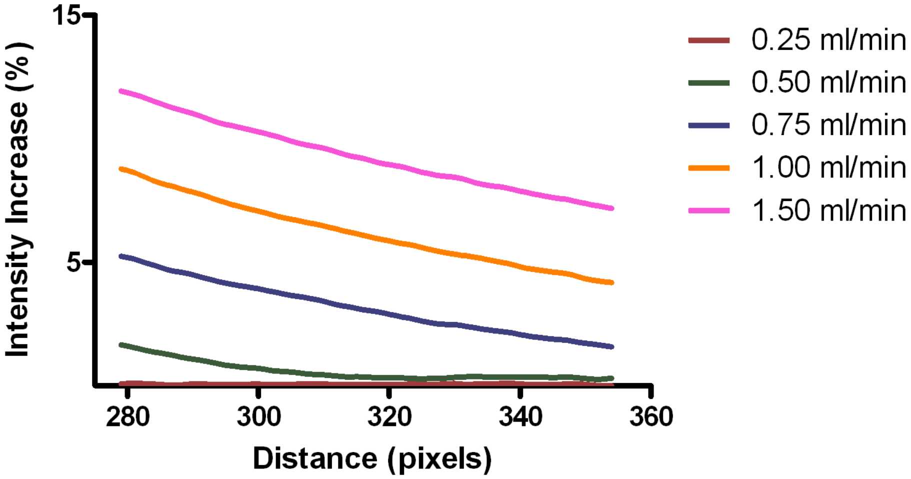

Figure 6.10: Intensity decay over distance for the hexagonal geometry

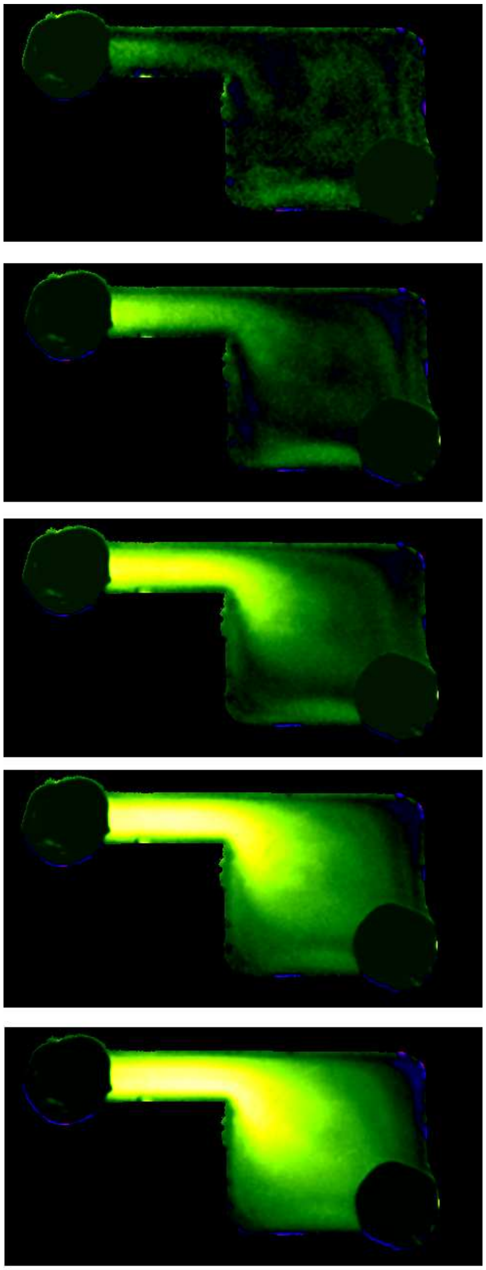

Figure 6.11: Flow images of the cleaver chamber. Flow rates: 0.25, 0.50, 0.75, 1.00, 1.50 ml/min (top to bottom).

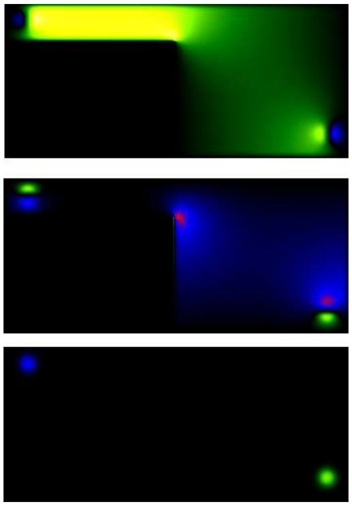

Figure 6.12: CFD flow images of the cleaver geometry for the x, y, z direction (top to bottom).

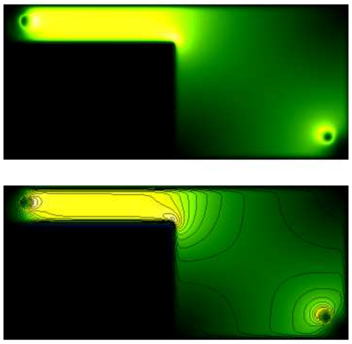

Figure 6.13: CFD flow magnitude images of the cleaver geometry without (top) and with contour lines (bottom)

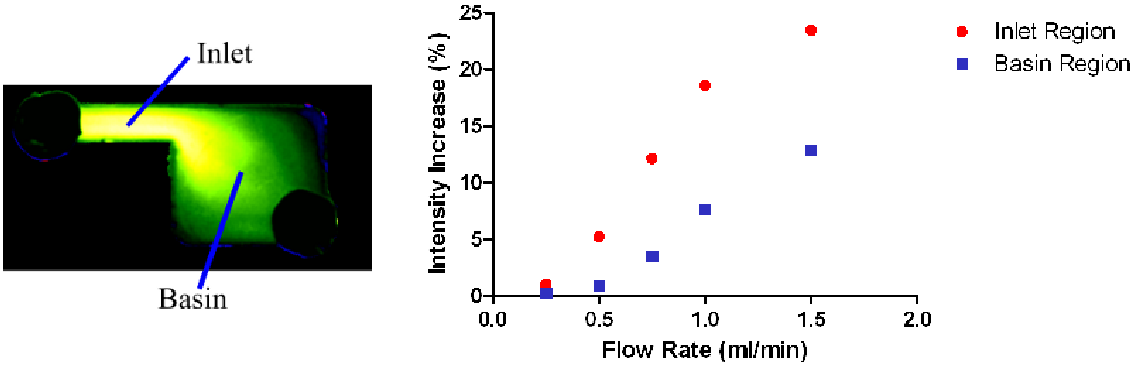

Figure 6.14: Flow rate vs. average intensity increase for the inlet and wide basin region of the cleaver geometry

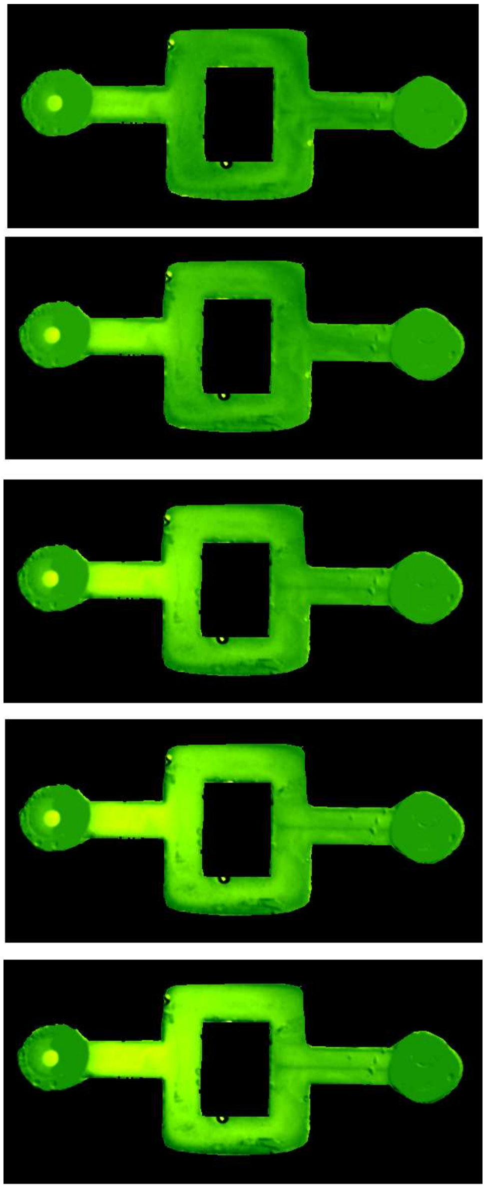

Figure 6.15: Flow images of the island geometry. Flow rates: 0.25, 0.50, 0.75, 1.00, 1.50 ml/min (top to bottom).

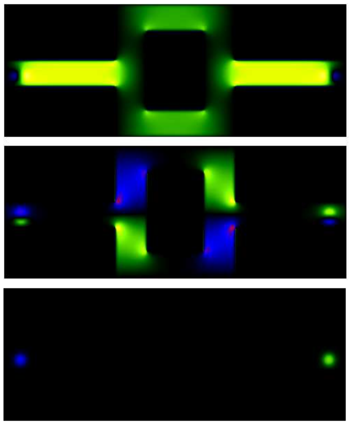

Figure 6.16: CFD flow images of the island geometry for the x, y, z direction (top to bottom).

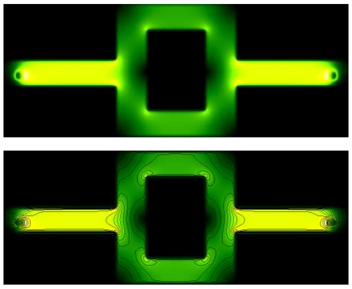

Figure 6.17: CFD flow magnitude images of the island geometry without (top) and with contour lines (bottom)

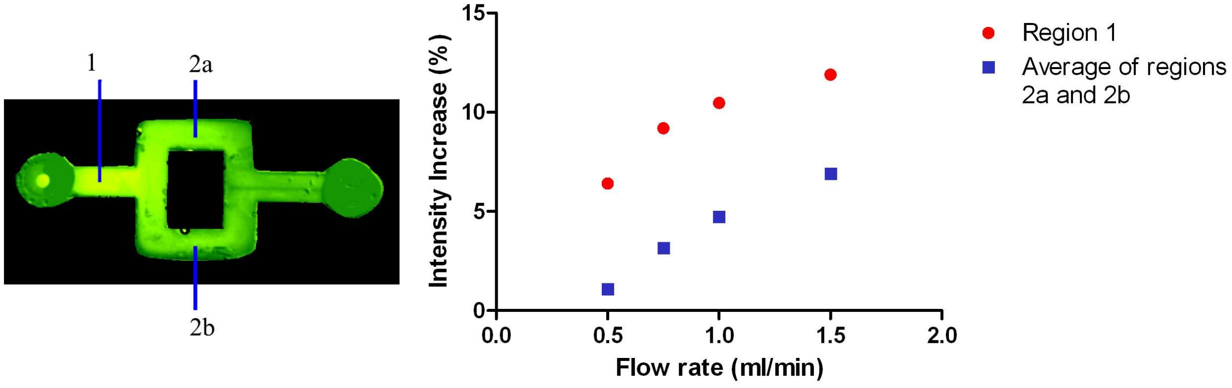

Figure 6.18: Flow rate vs. intensity increase for region 1 and average of regions 2a and 2b of the island geometry

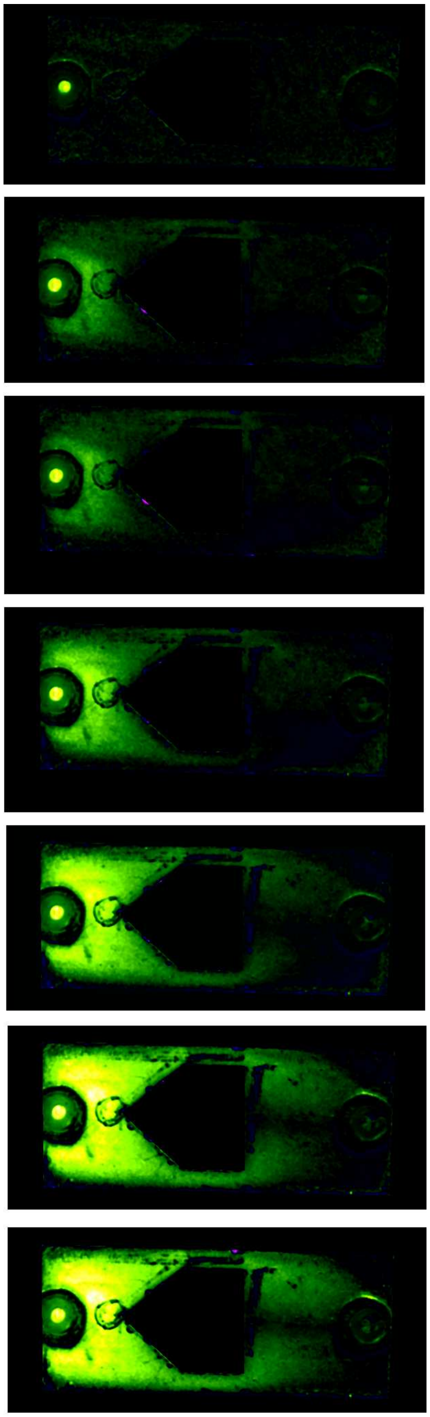

Figure 6.19: Flow images of the pentaisland geometry. Flow rates: 0.25, 0.50, 0.75, 1.00, 1.50, 2.00, 2.50 ml/min (top to bottom).

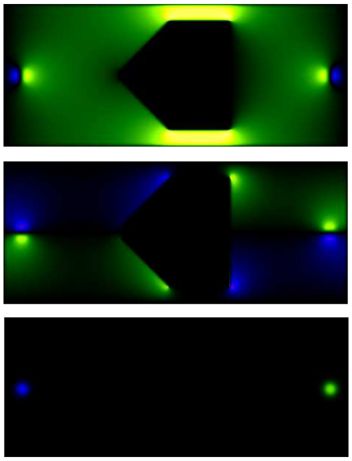

Figure 6.20: CFD flow images of the pentaisland geometry for the x, y, z direction (top to bottom).

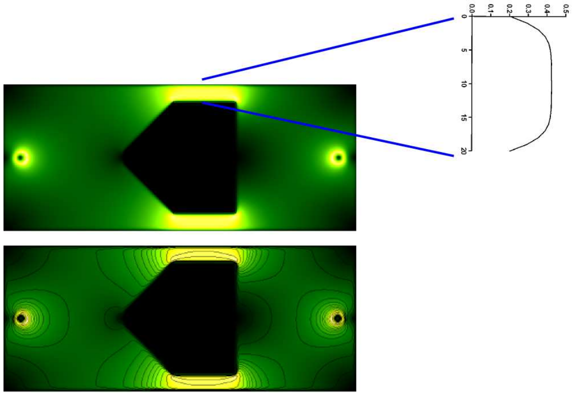

Figure 6.21: CFD flow magnitude images of the pentaisland geometry without (top) and with contour lines (bottom)

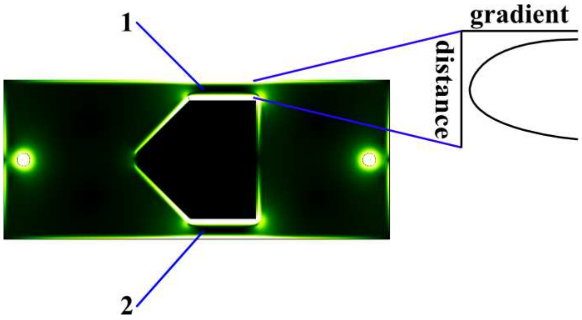

Figure 6.22: Shear stress magnitude of the pentaisland chamber

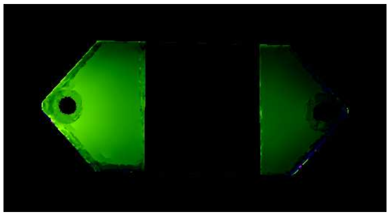

Figure 6.23: Flow images of the hexagonal geometry at 1.50 ml/min, with paper placed in the middle

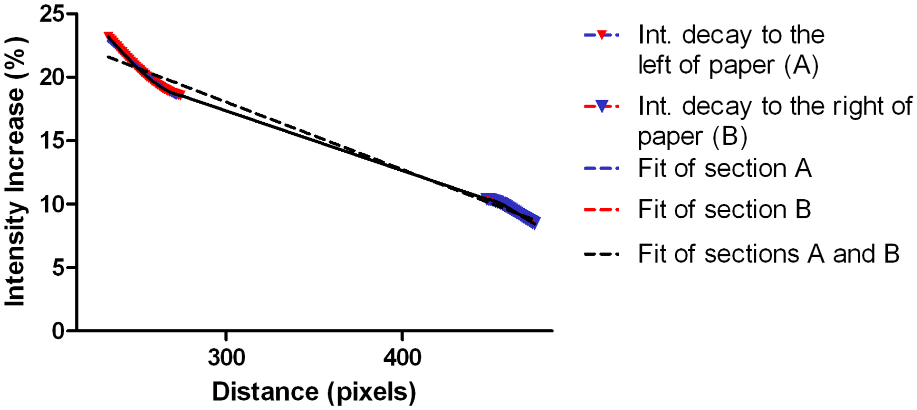

Figure 6.24: Intensity decay over distance for the flow image of the hexagonal geometry with paper placed in the middle. Linear regression values for: Region A (slope=-0.12, R^2=0.98), Region B (slope=-0.08, R^2=0.99), Regions A and B (slope=-0.05, R^2=0.99).

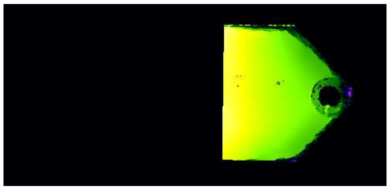

Figure 6.25: Flow images of the hexagonal geometry at 1.50 ml/min, with paper covering half of the geometry to the left

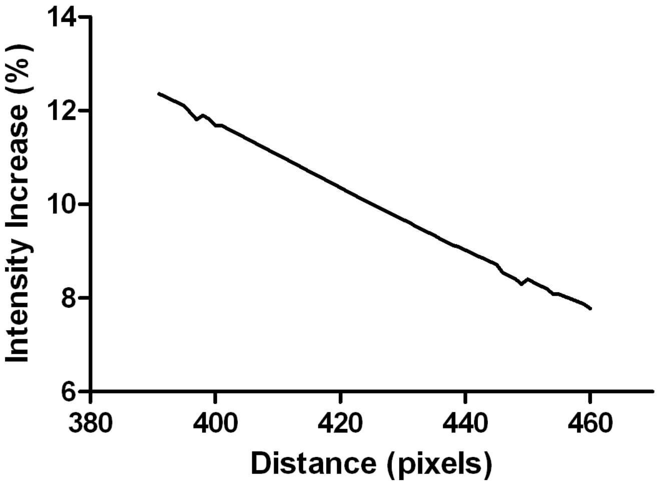

Figure 6.26: Intensity decay over distance for the flow image of the hexagonal geometry with paper covering half of the geometry to the left

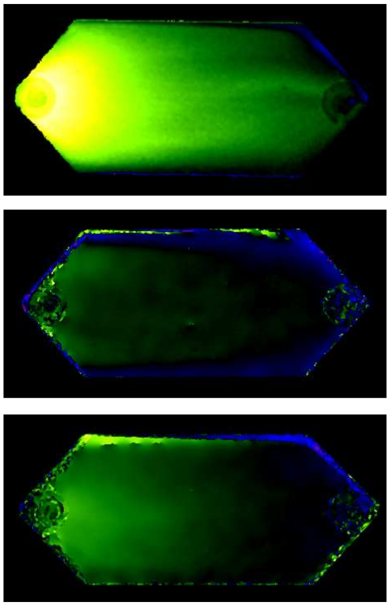

Figure 6.27: Flow images of the hexagonal geometry at 1.50 ml/min, with CCVJ in ethylene glycol (top), CCVJ-TEG in ethylene glycol (middle), Diol in ethylene glycol (bottom)

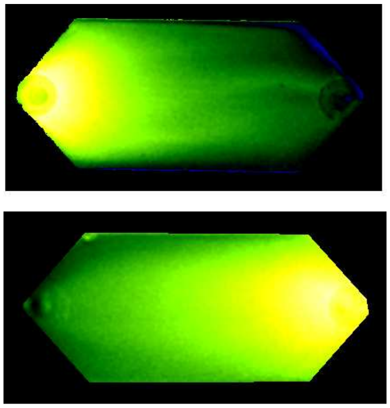

Figure 6.28: Flow images of the hexagonal geometry at 1.50 ml/min, with fluid injected left to right (top), and fluid injected right to left (bottom)

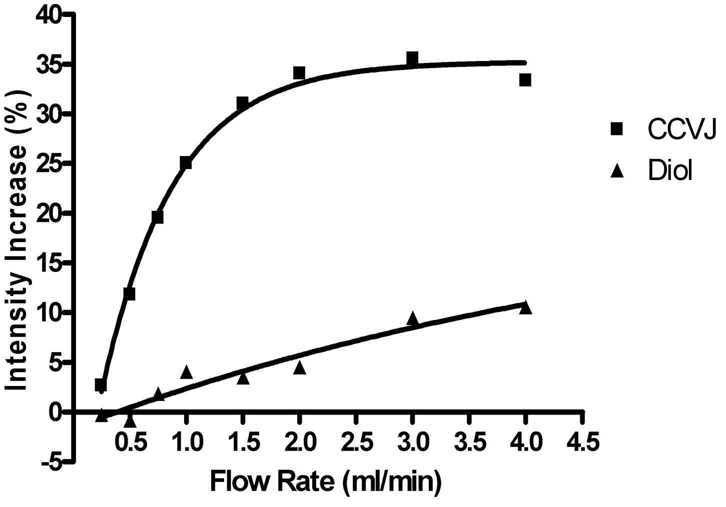

Figure 6.29: Flow rate vs. average intensity increase for CCVJ in EG, and Diol in EG in the central region of the hexagonal geometry

Chapter 7

Discussion

A method was developed and demonstrated to use fluorescent imaging to visualize flow patterns in flow channels of different geometries. The method was based on low-cost equipment. A pair of collimated high-power LED provided excitation light very similar to laser induced fluorescence (LIF), but with the LED's advantage to illuminate larger areas more homogeneously. Image acquisition was performed with a consumer-grade SLR camera which cost $\approx$ \$800, while the other scientific cameras were several thousand dollars more expensive. Before the SLR camera, several scientific cameras were tried, but found unsatisfactory in terms of sensitivity and integration time. The SLR camera, on the other hand, provided not only a long integration time of up to 30 seconds, which is much longer than the scientific cameras that were tested in this study, but also a wide range of sensitivity settings for the sensor which allow to select a suitable exposure (and integration) time.

The increased noise at higher sensitivity settings was eliminated by image processing: rank filtering, image averaging, and Gaussian filtering. The major disadvantage of the camera was its propensity to perform its own internal image enhancement, which was primarily driven by the scene. Only after turning off all automatic functions, from automatic exposure to automatic white-balance, quantitative comparison between images became possible. Furthermore, the SLR camera acquires a color image. The highest intensity was found in the blue channel at peak sensitivity wavelength of 450 nm, and therefore the blue channel was extracted and used exclusively in the image processing steps. Because the green channel's peak sensitivity was $\approx$ 550 nm, the 450 nm blue channel peak sensitivity captures the 484-486 nm range of rotor's emission much better. Addition of the green channel did not change the findings, and the red channel contained no image information.

From the images, it can be seen that molecular rotors in viscous solvents exhibited increased quantum yield when subjected to shearing without any wavelength peak shift, which can be seen in Figure 5.1 for a solution of CCVJ in ethylene glycol, and Figure 5.2 for Diol in ethylene glycol, thus establishing their unique property of shear sensitivity for these particular molecular rotors.

Increased shear is associated with increased intensity, but in a nonlinear fashion (saturation effects). Fitting of the regions for cleaver and island chambers with Equation 6.8, shows saturation in regions of high intensity. This observation is consistent with earlier findings in simple flow tubes. Generally, a mononomic nonlinearity in a sensor poses no problem as it can be calibrated with a suitable compensating calibration curve. However, two observations warrant further research: the comparison with CFD simulations and the conspicuous fading of the intensity.

A good match between computed flow magnitude in Figure 6.13 and fluorescence intensity was found in the cleaver geometry (Figure 6.11). In both cases, the intensity decay starts at the inflow area, and it's reduced in the wide basin area. Intensity increases in both regions with an increase in the flow rate (Figure 6.14). A good qualitative match exist with the CFD images.

For the island geometry shown in Figure 6.14, intensity is strongest in the narrow inflow channel and splits up in two as it reaches the rectangular island in the middle. Intensity average of the regions above and below the island are about half the intensity of the inflow channel. The two split streams join together as they enter the outflow channel. This is consistent with the intensity analysis of those regions, as shown in Figure 6.18, and match to the values from the CFD images.

In the pentaisland geometry (Figure 6.19), the CFD simulation of the shear sterss shows an intensity pattern above and below the island, which seemingly appears to be proportional to velocity rather than shear stress (Figure 6.21), which points to the phenomena of flow rather than shear stress. Moreover the CFD simulation for flow magnitude (Figure 6.21) shows a better match with intensity images from Figure 6.19. These findings stand in contrast of those by Haidekker et al, who hypothesized from experiments with fluids of different viscosity and flow gradients that the intensity increase is caused by shear stress rather than shear rate or flow [52].

The question whether fluid velocity or shear stress causes the intensity increase is fundamental to the understanding of the underlying mechanism of shear stress sensitivity, and these experiments point to flow. Further experiments would provide additional verification with the experimental part involving fluorescence and the other one with the simulation part. In the experimental part, fluids with different viscosities may provide evidence in favor of either flow or shear stress. The CFD simulations are idealizations and do not reflect small irregularities, where fluorescent images give the real flow patterns.

The question of fading also warrants closer inspection. No such effect was observed in the stirrer experiment or in the fiber/tube experiments reported by Haidekker et al. The fading occurred in all flow geometries, and reversing the direction also reversed the direction of fading (Figure 6.28), but not its effect, thus proving it's direction independent. Intensity decay as a function of distance for the hexagonal chamber in Figure 6.10, shows the fading occurring for all flow rates in a selected central region.

Additional experiments with a hexagonal flow geometry with the left partially occluded from light indicate that the fading starts only in the uncovered region, and the intensity values correspond to those of the uncovered hexagonal chamber shown in Figure 6.9. Covering only the midsection of the hexagonal geometry, and proceeding the with the usual experimental regimen of flow rates, shows a decaying trend even in the uncovered portion of the chamber, albeit with a smaller negative slope than the regions without any paper placed in front.

Pulsed excitation light in a wide frequency range, however, seems to have no effect on the fading. Also, geometric imperfections or other unanticipated effects of the flow chamber could be excluded since the chamber was tested with fluorescent microbeads (Figure 6.7). A hypothesis suggested that the excited state of CCVJ facilitates ester formation with the solvent alcohol. However, experiments involving a hydrophilic shear-sensitive ester, CCVJ triethyleneglycol ester, provide evidence against ester formation since CCVJ cannot form covalent bonds with the solvent, and all three dyes in ethylene glycol showed the same pattern of fading. Although the CCVJ/ethylene glycol and Diol/ethylene glycol solution could be examined for esters after the experiment, this approach appears to be less promising since the fading effect is reversible, and very unlikely to the cause of fading. Alternatively, non-covalent hydrogen bond formation may take place, facilitated by the excited state of the CCVJ molecule. In this case, fading should be seen even with CCVJ. Conversely, there should be no measurable fading in a polar but aprotic solvent where hydrogen formation cannot take place.

Different flow geometries exhibit different flow smoothness due to smaller cross section. which in turn lowers the Reynolds number, thus making it more laminar. In experiments with CCVJ in a low viscosity solvent, water, the intensity images didn't provide as much information and werent't as visually informative as CCVJ in ethylene glycol. Ethylene glycol is a polar protic solvent and its polarity also influences the underlying reaction mechanism with the dye, namely the bond formation, and by changing the solvent to polar aprotic, the reaction could be changed. An experiment was performed where a laser served as a point source excitation light. The results were inconclusive, but adjustment could be made to repeat it on a much longer and wider flow geometry, and compare it to the homogeneous LED light source for any differences.

Any potential temperature influence was excluded following several experiments calibrated to address the issue. Measurements of temperature increase caused by illumination on chamber showed variations less than 1 %. More so, intensity measurements of a central area in cleaver chamber geometry showed less than 1 % change, thus negating any warming of the fluid due to the light from the LEDs and potential change in solution viscosity.

Intensity and pattern visualizations were mainly observed in the x and y direction, but were hard to observe in the z direction because of the 2D nature of the image collection. Intensity images with CCVJ in EG were the best quality in terms of quantifying the average intensity, whereas images of CCVJ-TEG in EG and Diol in EG were of lesser sensitivity. This could potentially be enhanced with an increase in concentration.

These open questions non-withstanding, the experiments in this study give rise to an interesting and unique application of molecular rotors. Flow patterns can be imaged at extremely high resolutions (limited only by the resolution of the optical apparatus) and in real time (limited by the acquisition speed of the optical apparatus). Intensity changes were observed with flow rates as low as 0.25 ml/min which corresponds to less than 0.5 mm/s average velocity. This represents an extremely high sensitivity for a flow measurement system. This sensitivity cannot be matched by mainstream flow measurement methods such as Doppler ultrasound. Particle tracking can match the spatial resolution but has a slower temporal response. Flow meters of comparable sensitivity exist: they are based on a heated plate that gets cooled by the fluid flowing over the plate. Temperature measurement provides velocity. However, present commercial systems based on this principle cannot match the molecular rotor's spatial resolution.

The study of molecular rotors has various economic and engineering science benefits. Since molecular rotors have only recently been discovered as versatile mechanosensors in biology and engineering, current research provides a better insight into fundamental photophysical principles of molecular rotors. The engineering aspect of the study is the development of new methods to visualize flow patterns in real-time and on a microscopic scale. Commercially available techniques to image flow patterns such as Doppler Ultrasound and MRI are expensive, time consuming, have relatively low sensitivity and produce data of sometimes poor quality [49][55][56]. Molecular rotors promise to provide an alternative because they represent a new generation of extremely sensitive flow and shear sensors with low cost instrumentation, real-time high quality data acquisition. Potential applications can be found in the fields of micro- and nano- fludics, including mixing optimizations, flow measurement, closed loop flow control, flow and shear imaging, and the validation of computed fluid dynamics models. To further improve upon this technique, a more thorough understanding of the polar-polar interaction between molecular rotor and solvent is needed. To examine this, fluorescence under different shear regimes and different solvents needs to be tested.

Chapter 8

Conclusions And Future Research

8.1 Conclusions

Molecular rotors are viscosity sensitive flurophores whose emission intensity inreases in solvents when subjected to shearing. This particular phenomenon occurs in highly viscous solvents via a fluorescence emission pathway while the twisted intramolecular charge transfer states return to its ground state. Consequently this gives rise to a new method of imaging flow and shear stress on a microscopic scale with matchless sensitivity.

Examining the behavior of molecular rotor solutions in different geometries has shown the relation between fluorescence intensity and shear stress, following the real-time observation of flow patterns not possible with cumbersome methods as particle tracking. Fluorescence emission increases with flow rate increase, and similarities can be seen in computed fluid dynamic simulations of flow and shear stress. Intensity changes were observed with as low as 0.5 mm/s average flow velocity, which is extremely sensitive for a flow imaging apparatus.

Molecular rotors represent a new way of imaging flow patterns in real-time on a microscopic scale unlike commercially available alternatives of Doppler Ultrasound and MRI which are time consuming, expensive, posses low sensitivity and sometimes produce data of poor quality. This new method promises to provide an alternative with potential applications in micro- and nano-fluidics, fluid mixing optimizations, flow measurement, closed loop flow control, flow and shear imaging, and the validation of computed fluid simulations.

8.2 Future Research

The newly discovered property of molecular rotors as shear sensitive flow probes and their potential applications in microflow imaging represent an important new discovery, but some of their unexplained effects, such as quantum yield fading over distance, necessitate additional research. A thorough understanding of physical interactions between molecular rotors and solvent(s) is needed for further improvement and optimization of the technique. The hypothesis that polar-polar interaction of molecular rotors and solvents plays an important would involve examining fluorescence intensity increase under different shear regimes and different solvents.

Testing uses an already designed flow apparatus which provides for high-precision intensity measurement in a fluroscpectrometer. By applying a series of different flow rates, the intensity increase as a function of flow and viscosity can be obtained, and the three constants ($\Delta I_{max}, \eta_c, v_c$) determined by nonlinear regression. Constants will be obtained for different solvents shown in Table 8.1.

Table 8.1: Solvent Properties

Solvent	Viscosity η (m·Pas)	Polarity	Dielectric Constant ϵ
Water	1.00	Polar Protic	80.10
Ethanol	1.20	Polar Protic	25.00
Dimethylsulfoxide	2.47	Diolar Aprotic	48.90
Toluene	0.59	Non-polar	2.39

Primary solvents included in the study are: water, ethanol, dimethylsulfoxide, and toluene. Their viscosities range from low of 0.59 m·Pas for toluene to high of 2.47 m·Pas for dimethylsulfoxide, which causes different base quantum yields and is reflected in constant viscosity. Their respective dielectric constants (measure of sharing electrons) are highest for water, while it is lowest for toluene, which is esentially nonpolar. Another characteristic are distinctive types of polarities. Polar protic solvents (water, ethanol) posses a hydroxyl group and can donate hydrogen, allowing them to bond with solvent, while polar aprotic solvent (dimethylsulfoxide) lacks the hydroxyl group, thereby restricting its ability to bond with the hydrogen from the solvent. Different types of molecular rotors depending on polarity characterized by the number of hydroxyl groups (a molecular rotor with one OH group (CCVJ) is more polar than a molecular rotor with two OH groups (Diol)) used in conjuction with DCVJ (has CN group, thus it has no polarity) provide a diversity of shear sensitive reaction mechanisms.

Solutions of molecular rotors are injected into the flow system consiting of a quartz tubing (4 mm in diamater); quartz tubing inport is connected to the syringe via teflon tubing, while the outport is connected to an empty container to collect exiting fluid. Teflon is a type of plastic with superior qualities of resistance to highly reactive solvents, most particularly dimethylsulfoxide. Quartz tubing is held in place in a custom made holder, which is positioned in a FluoroMax Spectrofluorometer chamber. With a syringe pump and a glass syringe, different flow rates are applied (depending on the molecular rotor/solvent sensitivity), and emission intensity is recorded. An example of a resulting timecourse is shown in Figure 8.1 for CCVJ in ethylene glycol, and Figure 8.3 for Diol in ethylene glycol. A custom software is used to convert the timecourse data into date pairs of intensity increase over flow and perform nonlinear regression (shown in Figure 8.2 and 8.4), providing the v_c and ΔI_{max} in equation 6.8. From Figure 8.1 and 8.3, it can be seen that as the flow rate is increased, higher intensity can be observed, which corresponds to different shear sensitivity of CCVJ in EG and Diol in EG shown in the shear sensitivity section. Non-linear regression fit graphs shown in Figures 8.2 and 8.4 point to values of v_c which is higher for CCVJ in EG than for Diol in EG. The larger the value of v_c, the faster the viscous solution reach the saturation level, and this is seen in the graphs.

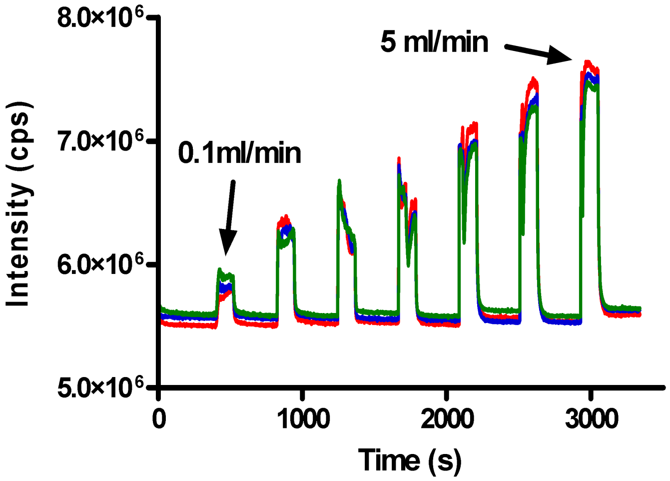

Figure 8.1: 10 μM CCVJ in Ethylene Glycol Timecourse (N=3)

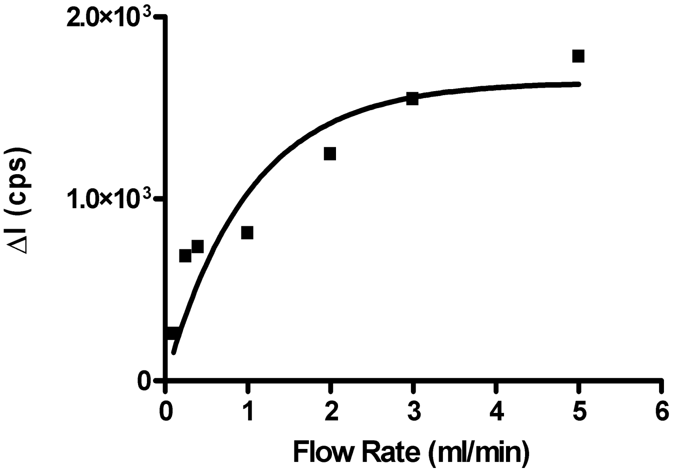

Figure 8.2: Nonlinear regression fit of timecourse data for 10 μM CCVJ in Ethylene Glycol

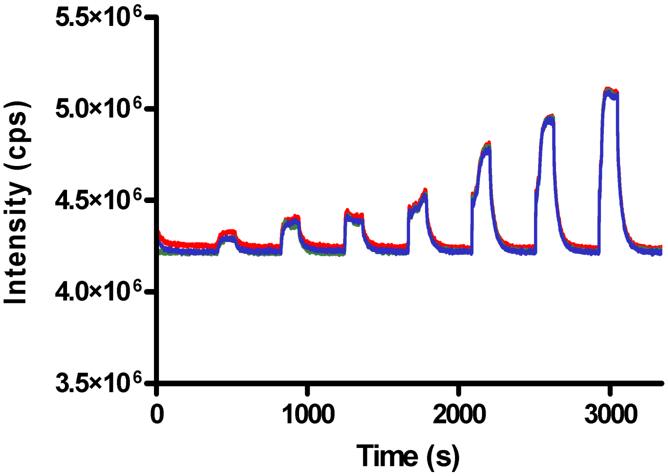

Figure 8.3: 10 μM Diol in Ethylene Glycol Timecourse (N=3)

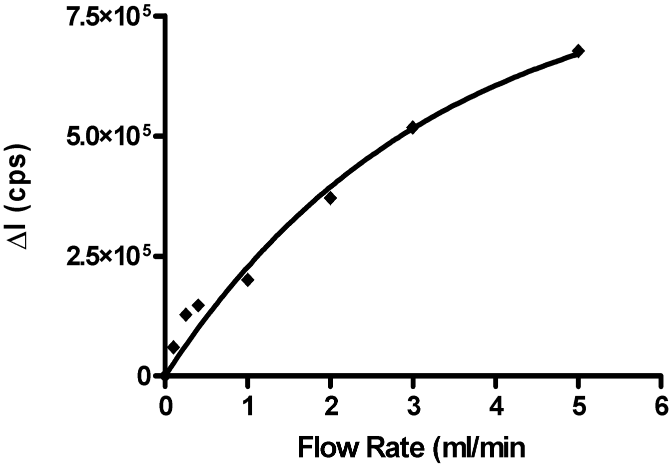

Figure 8.4: Nonlinear regression fit of timecourse data for 10 μM Diol in Ethylene Glycol

BIBLIOGRAPHY

[1] J. R. Lakowicz and B. R. Masters. Principles of fluorescence spectroscopy. *Journal of Biomedical Optics*, 13:029901, 2008.

[2] E. Lippert, W. Luder, and H. Boos. Advances in molecular spectroscopy, ed. by a. *Mangini (Pergamon, Oxford 1962) p*, 443, 1962.

[3] K. Rotkiewicz, K. H. Grellmann, and Z. R. Grabowski. Reinterpretation of the anomalous fluorescence of pn, n-dimethylaminobenzonitrile. *Chem. Phys. Lett*, 19:315–318, 1973.

[4] Y. Huang, T. Cheng, F. Li, C. Luo, C. H. Huang, Z. Cai, X. Zeng, and J. Zhou. Photophysical studies on the mono-and dichromophoric hemicyanine dyes ii. solvent effects and dynamic fluorescence spectra study in chloroform and in lb films. *Journal of Physical Chemistry B-Condensed Phase*, 106(39):10031–10040, 2002.

[5] J. M. Lang, Z. A. Dreger, and H. G. Drickamer. A high pressure study of the effect of viscosity on the light induced isomerization of dmabn in three linear alcohols, isobutanol and glycerol. *Chemical Physics Letters*, 243(1-2):78–84, 1995.

[6] T. Förster and G. Hoffmann. Effect of viscosity on the fluorescence quantum yield of some dye systems. *Z Phys Chem*, 75:63–76, 1971.

[7] T. Iwaki, C. Torigoe, M. Noji, and M. Nakanishi. Antibodies for fluorescent molecular rotors. *Biochemistry*, 32(29):7589–7592, 1993.

[8] M. A. Haidekker, N. L'Heureux, and J. A. Frangos. *American Journal of Physiology-Heart and Circulatory Physiology*, volume 278, chapter Fluid shear stress increases membrane fluidity in endothelial cells: a study with DCVJ fluorescence, pages 1269–1273. Am Physiological Soc, 2000.

[9] A. Grinvald, R. Hildesheim, I. C. Farber, and L. Anglister. Improved fluorescent probes for the measurement of rapid changes in membrane potential. *Biophysical Journal*, 39(3):301–308, 1982.

[10] B. Wandelt, P. Cywinski, G. D. Darling, and B. R. Stranix. Single cell measurement of micro-viscosity by ratio imaging of fluorescence of styrylpyridinium probe. *Biosensors and Bioelectronics*, 20(9):1728–1736, 2005.

[11] M. K. Kuimova, G. Yahioglu, J. A. Levitt, and K. Suhling. Molecular rotor measures viscosity of live cells via fluorescence lifetime imaging. *Journal of the American Chemical Society*, 130(21):6672–6673, 2008.

[12] R. L. Daugherty and J. B. Franzini. *Fluid mechanics with engineering applications.* McGraw-Hill, 1965.

[13] D. R. Lide. *CRC Handbook of Chemistry and Physics: A Ready-Reference Book of Chemical and Physical Data.* CRC press, 2008.

[14] A. E. Nikolaev, G. Myszkiewicz, G. Berden, W. L. Meerts, J. F. Pfanstiel, and D. W. Pratt. Twisted intramolecular charge transfer states: Rotationally resolved fluorescence excitation spectra of 4, 4-dimethylaminobenzonitrile in a molecular beam. *The Journal of chemical physics*, 122:084309, 2005.

[15] K. Dahl, R. Biswas, N. Ito, and M. Maroncelli. Solvent dependence of the spectra and kinetics of excited-state charge transfer in three (alkylamino) benzonitriles. *Journal of Physical Chemistry B-Condensed Phase*, 109(4):1563–1585, 2005.

[16] W. M. Kwok, C. Ma, D. Phillips, P. Matousek, A. W. Parker, and M. Towrie. Picosecond time-resolved study of 4-dimethylaminobenzonitrile in polar and nonpolar solvents. *J. Phys. Chem. A*, 104(18):4188–4197, 2000.

[17] H. Okamoto. Picosecond transient infrared spectrum of 4-(dimethylamino) benzonitrile in the fingerprint region. *J. Phys. Chem. A*, 104(18):4182–4187, 2000.

[18] E. T. J. Nibbering, H. Fidder, and E. Pines. Ultrafast chemistry: Using time-resolved vibrational spectroscopy for interrogation of structural dynamics. 2004.

[19] B. Bagchi. Isomerization dynamics in solution. *International Reviews in Physical Chemistry*, 6(1):1–33, 1987.

[20] W. Rettig. Solvent polarity dependent formation dynamics of tict states. i. differential solvato-kinetics. *Ber. Bunsenges. Phys. Chem*, 95:259, 1991.

[21] D. Braun and W. Rettig. Kinetic studies of twisted intramolecular charge transfer in highly viscous solvents as a function of pressure and temperature. *Chemical Physics*, 180(2):231–238, 1994.

[22] J. M. Hicks, M. T. Vandersall, E. V. Sitzmann, and K. B. Eisenthal. Polarity dependent barriers and the photoisomerization dynamics of molecules in solution. *Chem. Phys. Leii.*, 135:413–420, 1987.

[23] W. Rettig. Application of a simplified microstructural solvent interaction model to the solvatochromism of twisted intramolecular charge transfer (tict) states. *J. Mol. Struct*, 84((3-4)):303–327, 1982.

[24] A. Bhattacharya, S. Roy, and B. Bhattacharyya. Fluorescence energy transfer measurement of distances between ligand binding sites of tubulin and its implication for protein-protein interaction. *Protein Science*, 5(10), 1996.

[25] M. S. A. Abdel-Mottaleb, R. O. Loutfy, and R. Lapouyade. Non-radiative deactivation channels of molecular rotors. *J Photochem. Photobiol. A*, 48(1):87, 1989.

[26] M. A. Haidekker, T. P. Brady, D. Lichlyter, and E. A. Theodorakis. A ratiometric fluorescent viscosity sensor. *Journal of the American Chemical Society*, 128(2):398–399, 2006.

[27] M. E. Nipper, S. Majd, M. Mayer, J. C. M. Lee, E. A. Theodorakis, and M. A. Haidekker. Characterization of changes in the viscosity of lipid membranes with the molecular rotor fcvj. *BBA-Biomembranes*, 1778(4):1148–1153, 2008.

[28] F. Heisel, J. A. Miehe, and J. M. G. Martinho. p-dimethylaminobenzonitrile in polar solution. ii: Quantum yield measurements and quasi-stationary kinetic study of the electron transfer reaction. *Chemical physics*, 98(2):243–249, 1985.

[29] A. S. Klymchenko and A. P. Demchenko. Electrochromic modulation of excited-state intramolecular proton transfer: The new principle in design of fluorescence sensors. *J. Am. Chem. Soc*, 124(41):12372–12379, 2002.

[30] A. K. Doolittle. Studies in newtonian flow. iii. the dependence of the viscosity of liquids on molecular weight and free space (in homologous series). *Journal of Applied Physics*, 23:236, 1952.

[31] A. K. Doolittle and D. B. Doolittle. Studies in newtonian flow. v. further verification of the free-space viscosity equation. *Journal of Applied Physics*, 28:901, 1957.

[32] R. O. Loutfy and B. A. Arnold. Effect of viscosity and temperature on torsional relaxation of molecular rotors. *The Journal of Physical Chemistry*, 86(21):4205–4211, 1982.

[33] K. Y. Law. Fluorescence probe for microenvironments: anomalous viscosity dependence of the fluorescence quantum yield of pn, n-dialkylaminobenzylidenemalononitrile in 1-alkanols. *Chemical Physics Letters*, 75:545–549, 1980.

[34] A. Grinvald, A. Fine, I. C. Farber, and R. Hildesheim. Fluorescence monitoring of electrical responses from small neurons and their processes. *Biophysical Journal*, 42(2):195–198, 1983.

[35] M. Vogel and W. Rettig. Efficient intramolecular fluorescence quenching in triphenylmethane-dyes involving excited states with charge separation and twisted conformations. *Berichte der Bunsengesellschaft für Physikalische Chemie*, 89(9):962–968, 1985.

[36] M. A. Haidekker and E. A. Theodorakis. Molecular rotorsfluorescent biosensors for viscosity and flow. *Organic & Biomolecular Chemistry*, 5(11):1669–1678, 2007.

[37] A. Grinvald, A. Manker, and M. Segal. Visualization of the spread of electrical activity in rat hippocampal slices by voltage-sensitive optical probes. *The Journal of Physiology*, 333(1):269–291, 1982.

[38] B. Wandelt, P. Turkewitsch, B. R. Stranix, and G. D. Darling. Effect of temperature and viscosity on intramolecular charge-transfer fluorescence of a 4-p-dimethylaminostyrylpyridinium salt in protic solvents. *Journal of the Chemical Society. Faraday transactions*, 91(23):4199–4205, 1995.

[39] K. Luby-Phelps, S. Mujumdar, R. B. Mujumdar, L. A. Ernst, W. Galbraith, and A. S. Waggoner. A novel fluorescence ratiometric method confirms the low solvent viscosity of the cytoplasm. *Biophysical journal*, 65(1):236–242, 1993.

[40] P. Turkewitsch, B. Wandelt, R. R. Ganju, G. D. Darling, and W. S. Powell. Effect of nucleotides on the charge-transfer fluorescence of trans-4-(pn, n-dimethylaminostyryl)-n-vinylbenzylpyridinium chloride. *Chemical Physics Letters*, 260(1-2):142–146, 1996.

[41] P. Turkewitsch, B. Wandelt, G. D. Darling, and W. S. Powell. Fluorescent functional recognition sites through molecular imprinting. a polymer-based fluorescent chemosensor for aqueous camp. *Anal. Chem*, 70(10):2025–2030, 1998.

[42] D. Axelrod, D. E. Koppel, J. Schlessinger, E. Elson, and W. W. Webb. Mobility measurement by analysis of fluorescence photobleaching recovery kinetics. *Biophysical Journal*, 16(9):1055–1069, 1976.

[43] S. Sawada, T. Iio, Y. Hayashi, and S. Takahashi. Fluorescent rotors and their applications to the study of gf transformation of actin. *Analytical biochemistry*, 204(1):110–117, 1992.

[44] T. Furuno, R. Isoda, K. Inagaki, T. Iwaki, M. Noji, and M. Nakanishi. A fluorescent molecular rotor probes the kinetic process of degranulation of mast cells. *Immunology letters*, 33(3):285–288, 1992.

[45] L. Waite. *Applied biofluid mechanics.* McGraw-Hill Professional, 2007.

[46] R. Haaverstad, N. Vitale, O. Tjomsland, A. Tromsdal, H. Torp, and S. O. Samstad. *The Annals of thoracic surgery*, volume 74, chapter Intraoperative color Doppler ultrasound assessment of LIMA-to-LAD anastomoses in off-pump coronary artery bypass grafting, pages 1390–1394. Soc Thorac Surgeons, 2002.

[47] E. Mark, M. R. T. Haacke, and R. W. Brown. *Magnetic resonance imaging: physical principles and sequence design.* Wiley-Liss, 1999.

[48] D. A. Feinberg, L. E. Crooks, P. Sheldon, J. Hoenninger, J. Watts, and M. Arakawa. Magnetic resonance imaging the velocity vector components of fluid flow. *Magn Reson Med*, 2(6):555–566, 1985.

[49] L. Axel. Blood flow effects in magnetic resonance imaging. *American Journal of Roentgenology*, 143(6):1157–1166, 1984.

[50] C. D. Meinhart, S. T. Wereley, and J. G. Santiago. Micron-resolution velocimetry techniques. In *Laser Techniques Applied to Fluid Mechanics, Selected Papers from the Ninth International Symposium*, pages 57–70.

[51] T. V. McCaffrey and R. D. McCook. A thermal method for the determination of tissue blood flow. *Journal of Applied Physiology*, 39(1):170, 1975.

[52] M. A. Haidekker, W. Akers, D. Lichlyter, T. P. Brady, and E. A. Theodorakis. Sensing of flow and shear stress using fluorescent molecular rotors. *Sensor Letters*, 3:42–48, 2005.

[53] P. Perona and J. Malik. Scale-space and edge detection using anisotropic diffusion. *IEEE Transactions on Pattern Analysis and Machine Intelligence*, 12(7):629–639, 1990.

[54] M. Griebel, T. Dornseifer, and T. Neunhoeffer. Numerical simulation in fluid dynamics: A practical introduction. 1998. *SIAM, Philadelphia*, 1998.

[55] D. H. Evans, W. N. McDicken, R. Skidmore, and J. P. Woodcock. Doppler ultrasound: physics, instrumentation and clinical applications. 1989.

[56] R. Turner, D. Le Bihan, C. T. Moonen, D. Despres, and J. Frank. Echo-planar time course mri of cat brain oxygenation changes. *Magn Reson Med*, 22(1):159–166, 1991.

Appendix A

Excitation/Emission Graphs

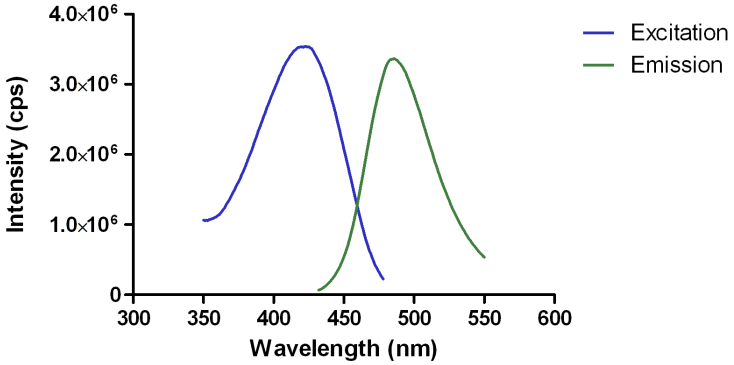

Figure A.1: 10 μM CCVJ in Ethylene Glycol Excitation and Emission Graph

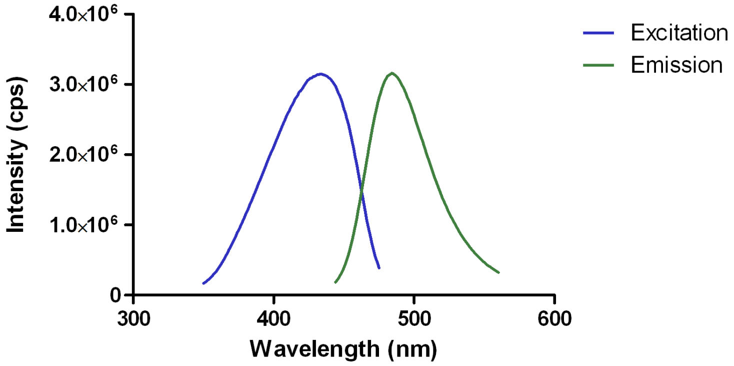

Figure A.2: 10 μM Diol in Ethylene Glycol Excitation and Emission Graph

Appendix B

Image Processing Macro Code

```
macro process:
    a = load (”nf0a.tif”);
    message (”load 1 done”);
    call (”preproc”);
    b1 = a;
    a = load (”nf0b.tif”);
    call (”preproc”);
    b2 = a;
    display (b1+b2);
    message (”No-flow done”);
    #flow rate 0.25 ml/min
    a = load (”f.25a.tif”);
    call (”preproc”);
    a250 = a;
    a = load (”f.25b.tif”);
    call (”preproc”);
    b250 = a;
    c250 = 100*(a250+b250-b1-b2)/(b1+b2);
    c250 = morph (c250, ”rank”, 8);
    save (c250,”ratio0250.tif”, ”tiff”);
    display (c250);
```

```
message (”250ul/min done”);
#flow rate 0.5 ml/min
a = load (”f.5a.tif”);
call (”preproc”);
a500 = a;
a = load (”f.5b.tif”);
call (”preproc”);
b500 = a;
c500 = 100*(a500+b500-b1-b2)/(b1+b2);
c500 = morph (c500, ”rank”, 8);
save (c500,”ratio0500.tif”, ”tiff”);
display (c500);
message (”500 ul/min done”);
#flow rate 0.75 ml/min
a = load (”f.75a.tif”);
call (”preproc”);
a750 = a;
a = load (”f.75b.tif”);
call (”preproc”);
b750 = a;
c750 = 100*(a750+b750-b1-b2)/(b1+b2);
c750 = morph (c750, ”rank”, 8);
save (c750,”ratio0750.tif”, ”tiff”);
display (c750);
message (”750 ul/min done”);
# flow rate 1.00 ml/min
a = load (”f1a.tif”);
```

```
    call (”preproc”);
    a1000 = a;
    a = load (”f1b.tif”);
    call (”preproc”);
    b1000 = a;
    c1000 = 100*(a1000+b1000-b1-b2)/(b1+b2);
    c1000 = morph (c1000, ”rank”, 8);
    save (c1000,”ratio1000.tif”, ”tiff”);
    display (c1000);
    message (”1 ml/min done”);
    # flow rate 1.50 ml/min
    a = load (”f1.5a.tif”);
    call (”preproc”);
    a1500 = a;
    a = load (”f1.5b.tif”);
    call (”preproc”);
    b1500 = a;
    c1500 = 100*(a1500+b1500-b1-b2)/(b1+b2);
    c1500 = morph (c1500, ”rank”, 8);
    save (c1500,”ratio1500.tif”, ”tiff”);
    display (c1500);
    message (”1.5 ml/min done”);
    endmacro;
procedure preproc:
    a = substack (a,1,1); # Extract green channel
    trim_image (a, 0,0,0, 4, 4095);
    setroi (358,1547,2356,1882);
```

```
    bkgnd = measure (a,0);
    setroi (); # reverse ROI
    a = a-bkgnd;
    a = morph (a,”rank”,8);
    a = morph (a,”rank”,8); # noise reduction
    a = resize (a, 752,500); # Scale down by factor of 4
    a = convolve (a, ”smooth”); # More noise reduction
    a = convolve (a, ”smooth”);
endproc;
macro postproc:
    a = load (”interactive”);
    a = morph (a,”rank”,8);
    trim_image (a, 1,1,0, 0, 0);
    display (a);
endmacro;
macro meas_cleaver:
    foreach (fn, ”ratio*.tif”);
    message (”loading ”,fn);
    img = load (fn);
    display (img);
    setroi (289,105,395,141);
    av1=measure (img,0);
    setroi (415,157,501,232);
    av2=measure (img,0);
    print (”Image ”,fn,” average channel=”,av1,” basin=”,av2);
    endfor;
endmacro;
```

```
macro cfd_composite:
    u=load(file.tif);
    v=load(file.tif);
    w=load(file.tif);
    a=u*u+v*v+w*w;
    b=power(a,0.5);
    display(b);
endmacro;
macro tiff_tc:
    dim (xdata[100],ydata[100]); k=0;
    foreach (fn, ”nf??.tif”);
    n=substring (fn,4,5);
    message (”opening ”,fn, ” number ”,n);
    a = load (fn);
    trim_image (a, 0,0,0, 4, 4095, 0,0);
    b = substack (a,1,1);
    display (b);
    setroi (1361,556,2181,1217);
    x = measure (b,0);
    print (” ”,n,” ”,x);
    xdata[k]=k+1;
    ydata[k]=x;
    k=k+1;
    end for;
    graph (k,xdata,ydata);
endmacro;
macro LED_timecourse:
```

```
    dim (gdata[50,3]);      i=0;
    foreach (fn, ”??.tif”);
    a = load (fn);
    trim_image (a, 0,0,0, 4, 4095);
    b = substack (a,1,1);
    save (b,fn+”green.tif”,”tiff”);
    setroi (1840,570,2230,980);
    av = measure (b,0);
    gdata[i,0]=i; gdata[i,1]=av;
    b = substack (a,2,2);
    setroi (1840,570,2230,980);
    av = measure (b,0);
    gdata[i,2]=av;
    i=i+1;
    display (b);
    endfor;
    graph (i,gdata);
endmacro;
```

APPENDIX C

SOLVENT PROPERTIES

Table C.1: Solvent Properties. Adapted from [13]

Solvent	Chemical Formula	Viscosity η (m·Pas) at 25°C	Dielectric Constant ϵ
1-butanol	$C_4H_{10}O$	2.54	17.84
2-butanol	$C_4H_{10}O$	3.10	17.26
Ethanol	$C_5H_{12}O$	1.074	25.30
Methanol	CH_3OH	0.544	33
1-pentanol	$C_5H_{12}O$	3.62	15.13
2-pentanol	$C_5H_{12}O$	3.47	13.71
3-pentanol	$C_5H_{12}O$	4.15	13.35
1-Nonanol	$C_9H_{20}O$	9.12	8.83
Glycerol	$C_3H_8O_3$	934	47.2
Ethylene Glycol	$C_2H_6O_2$	16.06	41.4
Water	H_2O	1.00	80.10
Dimethylsulfoxide	$(CH_3)_2SO$	2.47	48.90
Toluene	$CH_3C_6H_5$	0.59	2.39